

# JGR Solid Earth

## RESEARCH ARTICLE

10.1029/2022JB025388

### Key Points:

- Two new eclogites in Mongolia record peak conditions between 560 and 715°C and 2.0–2.2 GPa at ~520 Ma
- >1,000 km Cambrian eclogite-bearing high-pressure metamorphic belt in the Central Asian Orogenic Belt
- The Cambrian eclogites record the closure of the Pan-Rodinnian Mirovoi Ocean

### Supporting Information:

Supporting Information may be found in the online version of this article.

### Correspondence to:

M. Zhu,  
[zhumingshuai@mail.iggcas.ac.cn](mailto:zhumingshuai@mail.iggcas.ac.cn)

### Citation:

Zhu, M., Zhang, F., Smit, M. A., Pastor-Galán, D., Guilmette, C., Miao, L., et al. (2023). Discovery of a >1,000 km Cambrian eclogite-bearing high-pressure metamorphic belt in the Central Asian Orogenic Belt: Implications for the final closure of the Pan-Rodinnian Ocean. *Journal of Geophysical Research: Solid Earth*, 128, e2022JB025388. <https://doi.org/10.1029/2022JB025388>

Received 15 AUG 2022

Accepted 31 DEC 2022

### Author Contributions:

**Conceptualization:** Mingshuai Zhu, Fuqin Zhang, Matthijs A. Smit, Daniel Pastor-Galán, Carl Guilmette, Laicheng Miao  
**Data curation:** Mingshuai Zhu, Yi Zou  
**Formal analysis:** Mingshuai Zhu, Shunhu Yang, Zeli Wang  
**Investigation:** Mingshuai Zhu, Fuqin Zhang, Laicheng Miao, Shunhu Yang, Ariuntsetseg Ganbat  
**Methodology:** Mingshuai Zhu, Yi Zou  
**Supervision:** Mingshuai Zhu, Fuqin Zhang, Matthijs A. Smit, Daniel Pastor-Galán, Carl Guilmette, Laicheng Miao, Yi Zou, Lorraine Tual  
**Validation:** Mingshuai Zhu, Matthijs A. Smit, Yi Zou  
**Visualization:** Mingshuai Zhu, Ariuntsetseg Ganbat  
**Writing – original draft:** Mingshuai Zhu, Fuqin Zhang, Matthijs A. Smit

© 2023. American Geophysical Union.  
 All Rights Reserved.

## Discovery of a >1,000 km Cambrian Eclogite-Bearing High-Pressure Metamorphic Belt in the Central Asian Orogenic Belt: Implications for the Final Closure of the Pan-Rodinnian Ocean

Mingshuai Zhu<sup>1,2</sup> , Fuqin Zhang<sup>1,2</sup>, Matthijs A. Smit<sup>3</sup>, Daniel Pastor-Galán<sup>4,5</sup>, Carl Guilmette<sup>6</sup> , Laicheng Miao<sup>1,2</sup>, Yi Zou<sup>1</sup>, Shunhu Yang<sup>1,2</sup> , Ariuntsetseg Ganbat<sup>7</sup> , Lorraine Tual<sup>3</sup>, and Zeli Wang<sup>8</sup>

<sup>1</sup>Key Laboratory of Mineral Resources, Institute of Geology and Geophysics, Chinese Academy of Sciences, Beijing, China, <sup>2</sup>Institutions of Earth Science, Chinese Academy of Sciences, Beijing, China, <sup>3</sup>Department of Earth, Ocean and Atmospheric Sciences, University of British Columbia, Vancouver, BC, Canada, <sup>4</sup>Department of Geodynamics, Universidad de Granada, Granada, Spain, <sup>5</sup>Frontier Research Institute for Interdisciplinary Sciences, Tohoku University, Sendai, Japan, <sup>6</sup>Département de Géologie et de Génie Géologique, E4m, Université Laval, Québec, QC, Canada, <sup>7</sup>Department of Earth Sciences, The University of Hong Kong, Hong Kong, China, <sup>8</sup>Shandong Key Laboratory of Depositional Mineralization and Sedimentary Minerals, Shandong University of Science and Technology, Qingdao, China

**Abstract** The immense Central Asian Orogenic Belt (CAOB) records the transition from the Pan-Rodinnian Mirovoi Ocean to the Paleo-Asian Ocean, but the final closure of the Mirovoi Ocean remains unexplored. Here we document two new eclogite occurrences, located between CAOB microcontinents and the Ediacaran–Cambrian island arc in Mongolia. Pseudosection modeling and geothermobarometry constrain peak conditions of ~560°C and ~2.2 GPa for the Urgamal eclogite and ~715°C and ~2.0 GPa for the Tsengel eclogite. Zircon U–Pb dating results suggest the Urgamal eclogite-facies metamorphism occurred at ~522 Ma, and the granite gneiss enclosing the eclogite yielded ~811 Ma crystallization age and ~519 Ma metamorphic age. Detrital zircon age spectra of the paragneisses associated with the eclogite suggest a probable provenance from the adjacent Zavkhan microcontinent and the Neoproterozoic arc superimposed on the microcontinent. The Tsengel eclogite has a protolith age of ~853 Ma and an eclogite-facies metamorphic age of ~522 Ma, and the associated migmatite gneiss record a ~520 Ma migmatization event. The rock associations and geochemical affinities indicate that their protoliths represent mafic rocks formed in a continental rift setting and the Early Neoproterozoic subduction–accretion complex, respectively. Their similar tectonic position and metamorphic age suggest that these rocks are part of a single >1,000 km long Cambrian high-pressure metamorphic belt. The rocks record closure of the Mirovoi Ocean within the CAOB and constrain this crucial event to ~520 Ma along the western margin of the microcontinents in Mongolia.

**Plain Language Summary** The history of the Mirovoi Ocean surrounding the Rodinia supercontinent is fundamental to understanding Earth's evolution during the Proterozoic and the supercontinent cycle. The Central Asian Orogenic Belt (CAOB), one of the largest accretionary orogens worldwide, records the transition from the Mirovoi Ocean to the Paleo-Asian Ocean. In this paper, we document two new Cambrian (514–522 Ma) continent-type eclogite occurrences in Mongolia that record metamorphic conditions of 560–715°C and 2.0–2.2 GPa (equivalent to ~60–~70 km depth). We propose that these eclogites were part of a single >1,000 km long Cambrian HP metamorphic belt, which recorded the closure of the Mirovoi Ocean within the CAOB.

## 1. Introduction

Repeated cycles of supercontinent amalgamation and dispersal have had a profound impact on the evolution of Earth systems at least since the end of the Archean (e.g., Condie, 2002; Mitchell et al., 2021; Nance et al., 2014; Pastor-Galán et al., 2019). Rodinia supercontinent is proposed to have been surrounded by a Panthalassa-like Pan-Rodinnian Ocean (known as the Mirovoi Ocean) during much of the Neoproterozoic (e.g., Hoffman, 1991; Zhao et al., 2018). While most studies have focused on the Rodinia continental configuration (e.g., Z. X. Li et al., 2008; Wen et al., 2018), the consumption and final closure of the Mirovoi Ocean is often overlooked, in spite of its crucial role in reconstructing the geodynamic processes of supercontinent

**Writing – review & editing:** Mingshuai Zhu, Fuqin Zhang, Matthijs A. Smit, Daniel Pastor-Galán, Carl Guilmette, Laicheng Miao, Shunhu Yang, Ariuntssetseg Ganbat, Lorraine Tual, Zeli Wang

cycle (Merdith et al., 2021; Murphy & Nance, 2003). The Central Asian Orogenic Belt (CAOB) is one of the largest accretionary collages worldwide, formed through multiple convergence and collisional events of various orogenic components from 1000 to 250 Ma (e.g., Windley et al., 2007; Xiao et al., 2015). The presence of early Neoproterozoic ophiolites (~1020–892 Ma; e.g., Buriánek et al., 2017; Gordienko et al., 2010; Khain et al., 2002) and subduction-related arc-rock assemblages (~1017–780 Ma; e.g., Buriánek et al., 2017; Kuzmichev & Larionov, 2011; Kuzmichev et al., 2005; H. Yang et al., 2020) indicate that before Rodinia break-up, the early CAOB was facing the Mirovoi Ocean (e.g., Buriánek et al., 2017; Kovach et al., 2021). The second stage of the CAOB (Altaids) formation corresponds with the evolution of the Paleo-Asian Ocean between 600 and 250 Ma (Şengör et al., 1993; Wilhem et al., 2012), which probably opened by the breakup of Rodinia (e.g., Cawood et al., 2007; Gladkochub et al., 2019; Z. X. Li et al., 2008; Zhao et al., 2018). However, the superposition and transition between the Mirovoi Ocean and Paleo-Asian Ocean tectonic domains remain enigmatic, mainly due to the poor constraints for the timing and location of the final closure of the Mirovoi Ocean within the CAOB.

Eclogites are robust markers for existence of convergent plate boundaries, and constrain the role of subduction, collision and exhumation processes of orogens (e.g., Tsujimori et al., 2006; Wei & Clarke, 2011). In particular, continental-type eclogites, that is, metamorphosed from continental protoliths, could provide robust constraints on the timing of the ocean closure and associated continent-continent or continent-arc collision (e.g., Gee et al., 2012; Hermann & Rubatto, 2014). In this contribution, we document two new Cambrian HP eclogites (Urgamal eclogite and Tsengel eclogite) in North Mongolia (Figures 1 and 2). Field, geochemical, geochronological and magnetic data indicate that a >1,000 km Cambrian HP metamorphic belt occurs along the west margin of the microcontinents in Mongolia. These findings provide key constraints about the closure of the Mirovoi Ocean, and on the tectonic evolution of the CAOB during the Neoproterozoic-Cambrian.

## 2. Geological Background and Samples

### 2.1. Regional Setting

The CAOB is bound by the Siberian Craton to the north and the Tarim-North China Craton to the south and is located between the Uralides in the west and the Pacific margin in the east (e.g., Xiao et al., 2015). The geology of Mongolia, in the heart of the CAOB, has been subdivided into two tectonic domains by the Main Mongolian Lineament, namely the “Caledonian” domain to the north and the “Hercynian” domain to the south (Figure 1; e.g., Badarch et al., 2002). The northern domain mainly consists of Precambrian microcontinents, Neoproterozoic-Cambrian subduction-accretionary complex, early Paleozoic metamorphic rocks and early Paleozoic basins with clastic rocks. In contrast, the southern domain is predominantly composed of mid to late Paleozoic island arc assemblages (Badarch et al., 2002; Windley et al., 2007).

The Urgamal eclogite occurs at the junction between the Zavkhan microcontinent and the Lake Zone arc, about 25 km south of the Urgamal town, Mongolia (Figures 1 and 2a). The basement of the Zavkhan microcontinent consists of Paleoproterozoic orthogneisses (~1.97 Ga) that are overlain and intruded by early Neoproterozoic (~960–787 Ma) igneous rocks (e.g., Badarch et al., 2002; Bold, Crowley, et al., 2016; Kovach et al., 2021). These early Neoproterozoic rocks are interpreted to be related to the subduction of the Mirovoi Ocean following the assembly of the Rodinia supercontinent (Kovach et al., 2021). The sequence was unconformably overlain by latest Ediacaran to Early Cambrian conglomerate, sandstone, argillite, glacial diamictite and limestone (e.g., Macdonald et al., 2009). A continental arc-derived eclogite has recently been reported in the Zavkhan microcontinent (Bayarbold et al., 2022; Kovach et al., 2021), but the protolith age and timing of the HP metamorphism are not well constrained. The Lake Zone arc mainly consists of calc-alkaline volcanic and sedimentary sequences with several ophiolite fragments, intruded by granitoids dated between 551 and 465 Ma (Jian et al., 2014; Yarmolyuk et al., 2011). The ophiolites (Dariv and Khantaishir; Figure 1) expose a complete stratigraphy and have been dated by the zircon U-Pb method as late Neoproterozoic (~560–570 Ma) (e.g., Dijkstra et al., 2006; Jian et al., 2014; Khain et al., 2003). The lavas and dikes within the ophiolites show boninitic affinity and thus interpreted to be formed within intraoceanic forearc environment (Dijkstra et al., 2006; Jian et al., 2014).

The Tsengel retrogressed eclogite is located near the boundary of the Tarvagatay microcontinent and the Dzhiba arc, about 20 km northeast of the Tosontsengel city, Mongolia (Figures 1 and 2b). The Tarvagatay microcontinent is enclosed by the Permian-Triassic igneous belt and consists of ~2.5–1.8 Ga gneiss, migmatite, amphibolite and

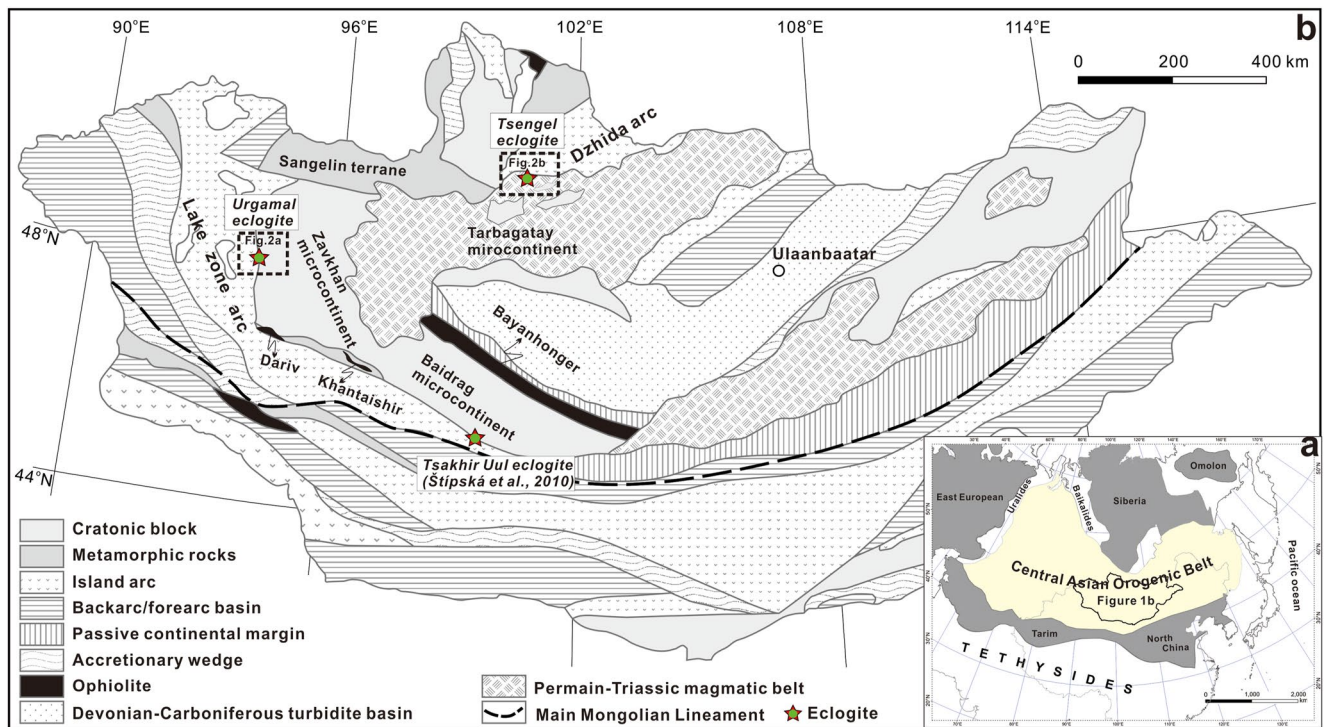


Figure 1. Tectonic map showing the main tectonic units of Mongolia (modified from Badarch et al. (2002)).

schist, intruded by ~770–800 Ma granites (e.g., Kozakov et al., 2011; Kröner et al., 2015). These rocks are overlain by Neoproterozoic-Lower Cambrian stromatolitic carbonate and volcanoclastic rocks (Badarch et al., 2002). The Dzhida arc is mainly composed of Ediacaran-Cambrian oceanic island arcs, oceanic islands (seamounts) and flysch complexes intruded by Ordovician granodiorites (e.g., Gordienko et al., 2015; Simonov et al., 2014). The oceanic island arc complexes mainly contain boninite, dismembered ophiolite, basalt-andesite, carbonate, tuff, and plagiogranite-diorite assemblages, and ~570–560 Ma gabbro and tonalite (Gordienko et al., 2015). The

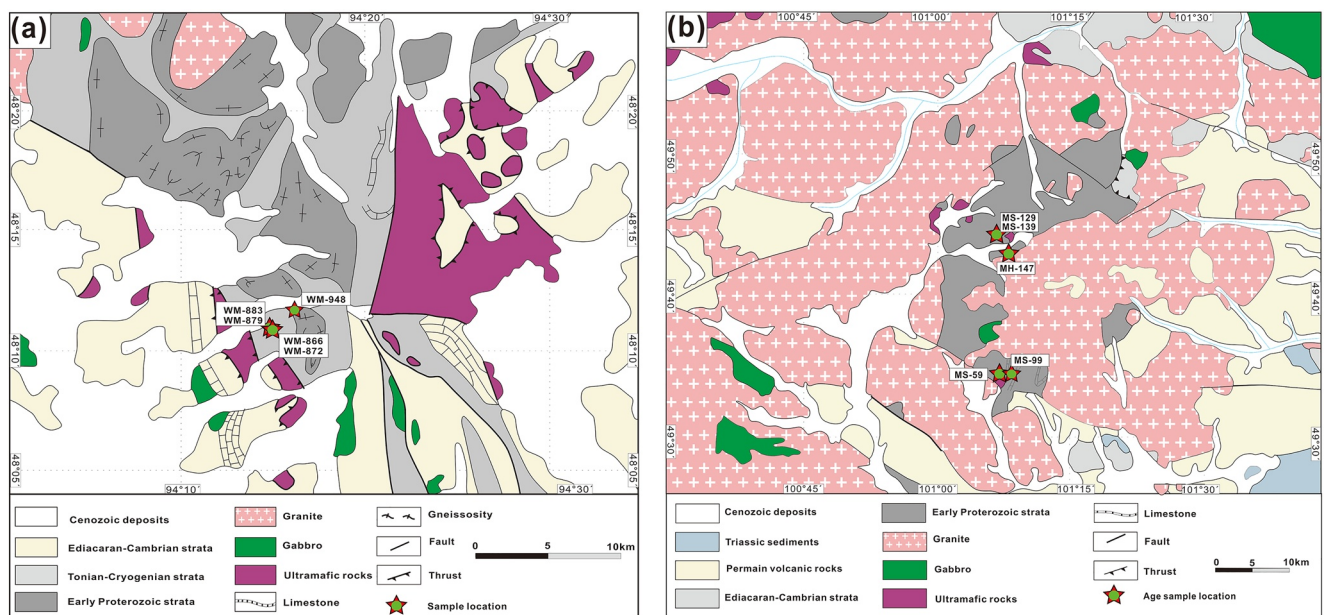


Figure 2. Geological map of the two eclogites in Mongolia. (a) The Urgamal eclogite studied area. (b) The Tsengel eclogite studied area.

boninite (Simonov et al., 2014) yielded a U-Pb age of  $542.1 \pm 4.2$  Ma (Tomurhuu et al., 2007). The oceanic island complex (seamount) is composed of several imbricated slices and nappes, with low-Ti tholeiite basalts in the lower thrusts, subalkaline high-Ti basalt-andesite with limestones and silicic strata structurally overlain by, and by dolomites and volcanoclastics in the upper thrusts (Gordienko et al., 2007). The flysch complex mainly consists of terrigenous, carbonate, and olistostromal strata with double provenances of the island arc and the oceanic island (Gordienko et al., 2007).

## 2.2. Field Occurrence and Petrography

The Urgamal eclogites are exposed as boudins of several tens of centimeters to meters in length or dykes within the Proterozoic muscovite-quartz schist, marble and granite gneiss of the Zavkhan microcontinent (Figures 3a–3d) that are foliated (sub-) parallel to the regional trend ( $\sim 30^\circ/50^\circ\text{E}$ ). Most eclogites are strongly deformed and are retrogressed especially adjacent to the tectonic contact with the country rock. The meta-ultramafic rocks in this region are mainly serpentinized peridotites and occur in fault contact with the Proterozoic formations (Figure 2a). The Ediacaran–Cambrian formations are mainly composed of strongly deformed greenschist to lower amphibolite-facies meta-basalt, meta-andesite, limestone, chert, and chlorite-quartz schist with rare conglomerate beds.

Macroscopically, the Urgamal eclogites occur as fine-grained massive rocks. The eclogite is mainly composed of garnet ( $\sim 38\%$ ), omphacite ( $\sim 35\%$ ), symplectite ( $\sim 9\%$ ), quartz ( $\sim 10\%$ ), rutile ( $\sim 5\%$ ), phengite ( $\sim 2\%$ ), and minor amounts of zircon, ilmenite and apatite, estimated on the basis of BSE maps of whole thin sections. Garnet occurs as idiomorphic to hypidiomorphic porphyroblasts with a grain size of 0.2–0.8 mm (Figures 4a and 4b), and contains mineral inclusions of quartz, rutile, calcite, talc, magnetite, amphibole and paragonite (Figure 4c). Omphacite is hypidiomorphic intergrowing with garnet, typically 0.2–0.5 mm in width and 0.5–1.5 mm in length with inclusions of quartz, rutile, and apatite (Figures 4a and 4b). Omphacite grains show a moderate preferred orientation, and are partially replaced by amphibole and plagioclase (Figures 4d and 4e). Amphibole intergrowths with plagioclase occur as vermicular symplectite around omphacite and thin coronas around garnet (Figures 4c–4e). Rutile occurs as inclusions in garnet and omphacite, and as 0.1–0.3 mm grains in the matrix (Figures 4c and 4e). Phengite flakes, 0.1–0.5 mm in length, are present in the matrix (Figure 4d). The Urgamal eclogite (sample WM-948) preserves at least three stages of metamorphism: the first stage (prograde) is represented by the inclusion assemblage of amphibole( $\text{Amp}_1$ ) + paragonite (Pa) + calcite(Cal) + quartz( $\text{Qz}_1$ ) + rutile( $\text{Rt}_1$ ) within the cores of garnet porphyroblasts (Grt). The second stage (peak) is indicated by matrix minerals of omphacite( $\text{Omp}$ ) +  $\text{Qz}_2$  +  $\text{Rt}_2$  + phengite (Ph) plus the mantle to rim domains of garnet porphyroblasts. The third stage (retrograde) produced the local symplectites of  $\text{Amp}_2$  + Pl  $\pm$  clinopyroxene (Cpx) rimming the garnet or partially replacing omphacite.

The Tsengel eclogite mainly occurs as lenticular boudins, ranging from less than 1 m to several meters in length, enclosed by mica-feldspar-quartz schists, migmatitic gneiss and marbles of the Tarvagatay microcontinent (Figures 3e–3g) foliated with a strike  $\sim 60^\circ$  and a dip  $\sim 60^\circ\text{NW}$ . The eclogites are largely retrogressed to garnet amphibolite (Figure 3h) with relics of eclogite assemblages preserved only in central parts of the lenses. There are some meta-ultramafic rocks, including pyroxenite and serpentinized peridotite, distributed as blocks in the metasedimentary rocks in this region (Figure 2b). However, their original relationship with the retrogressed eclogite is unclear.

The Tsengel retrogressed eclogite is medium to fine-grained and has a porphyroblastic texture. Whole-thin section BSE maps show that the sample consists mainly of garnet ( $\sim 38\%$ ), epidote ( $\sim 19\%$ ), amphibole ( $\sim 16\%$ ), plagioclase ( $\sim 15\%$ ), quartz ( $\sim 5\%$ ), ilmenite ( $\sim 3\%$ ), and rutile ( $\sim 3\%$ ), with omphacite, sphene, apatite and zircon as accessory minerals. Garnet porphyroblasts are idiomorphic to hypidiomorphic with a grain size of 0.1–0.8 mm, and are mostly rimmed by amphibole and plagioclase (Figures 4f and 4g). The garnet contains mineral inclusions of quartz, rutile, amphibole and epidote (Figure 4h). Amphibole occurs not only as part of the plagioclase-amphibolite symplectite but also as coarse, subhedral grains around garnet (Figures 4f–4h). Epidote occurs also as porphyroblasts rimmed by amphibole and plagioclase, and contains mineral inclusions of rutile (Figure 4i). Rutile occurs as both inclusions in garnet and in the matrix, 0.01–0.1 mm in size (Figure 4h). Plagioclase is either intergrown with amphibole to constitute vermicular symplectite around garnet, or grown outside of epidote (Figures 4f–4i). Omphacite was only observed as inclusions in the epidote grains (Figure 4i). The Tsengel retrogressed eclogite (sample MS-139) preserves three mineral assemblages: a prograde mineral

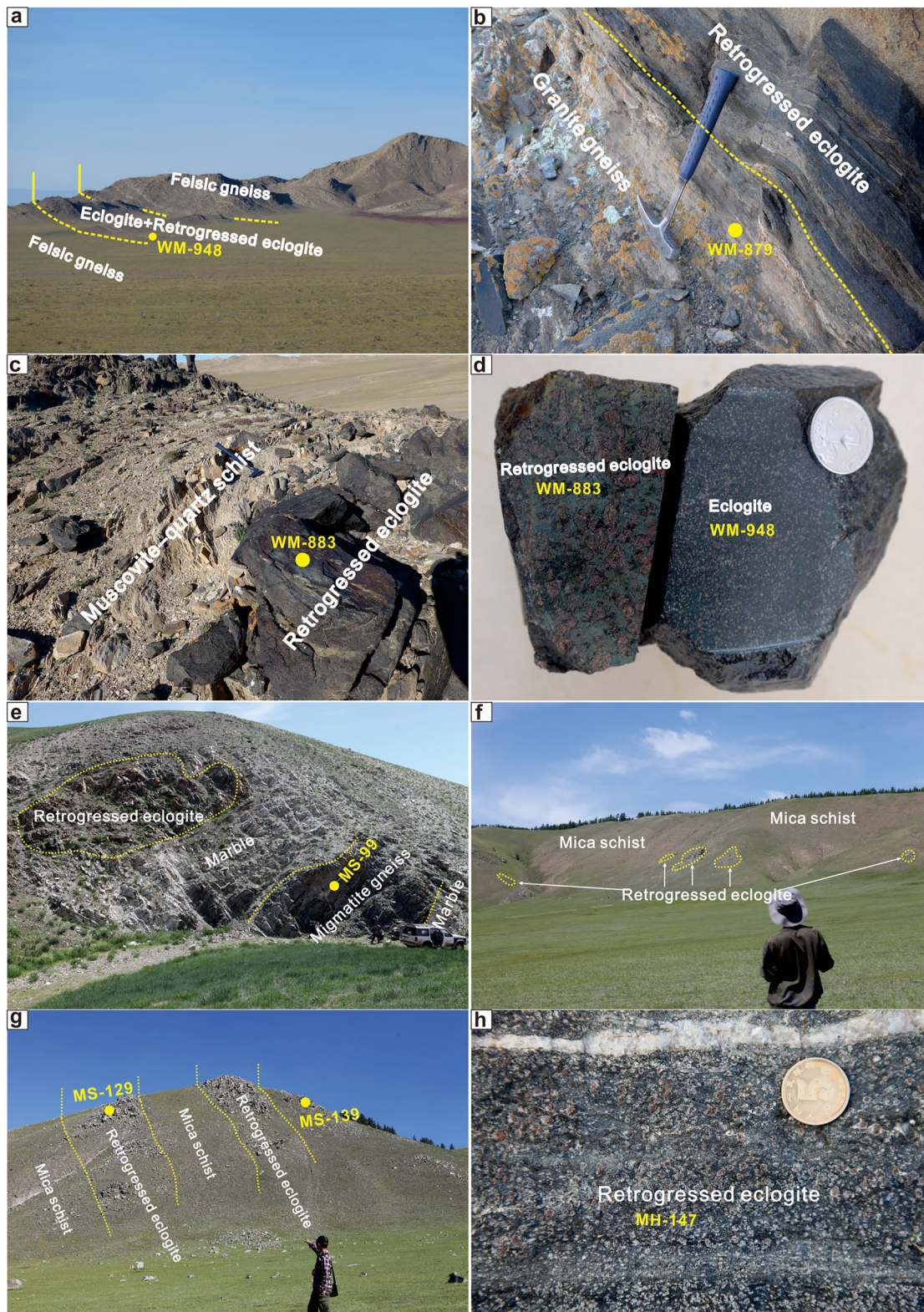


**Figure 3.** Field occurrences of the eclogites and its host rocks. (a) The Urgamal eclogite and retrogressed eclogite layers are enclosed in the felsic gneiss. (b) The Urgamal retrogressed eclogite as dyke-like bodies within the granitic gneisses. (c) The Urgamal lenticular retrogressed eclogite body in the muscovite-quartz schist. (d) Polished slab of the Urgamal eclogite and course-grained retrogressed eclogite. (e) The Tselgel retrogressed eclogites occur lens-like boudins in the marble and migmatite gneiss. (f) The Tselgel retrogressed eclogites occur as lens within the mica-quartz schists. (g) The Tselgel retrogressed eclogites occur as lens within muscovite-quartz schist. (h) The Tselgel retrogressed eclogites with a quartz vein show decompression texture of “white eye socket.”

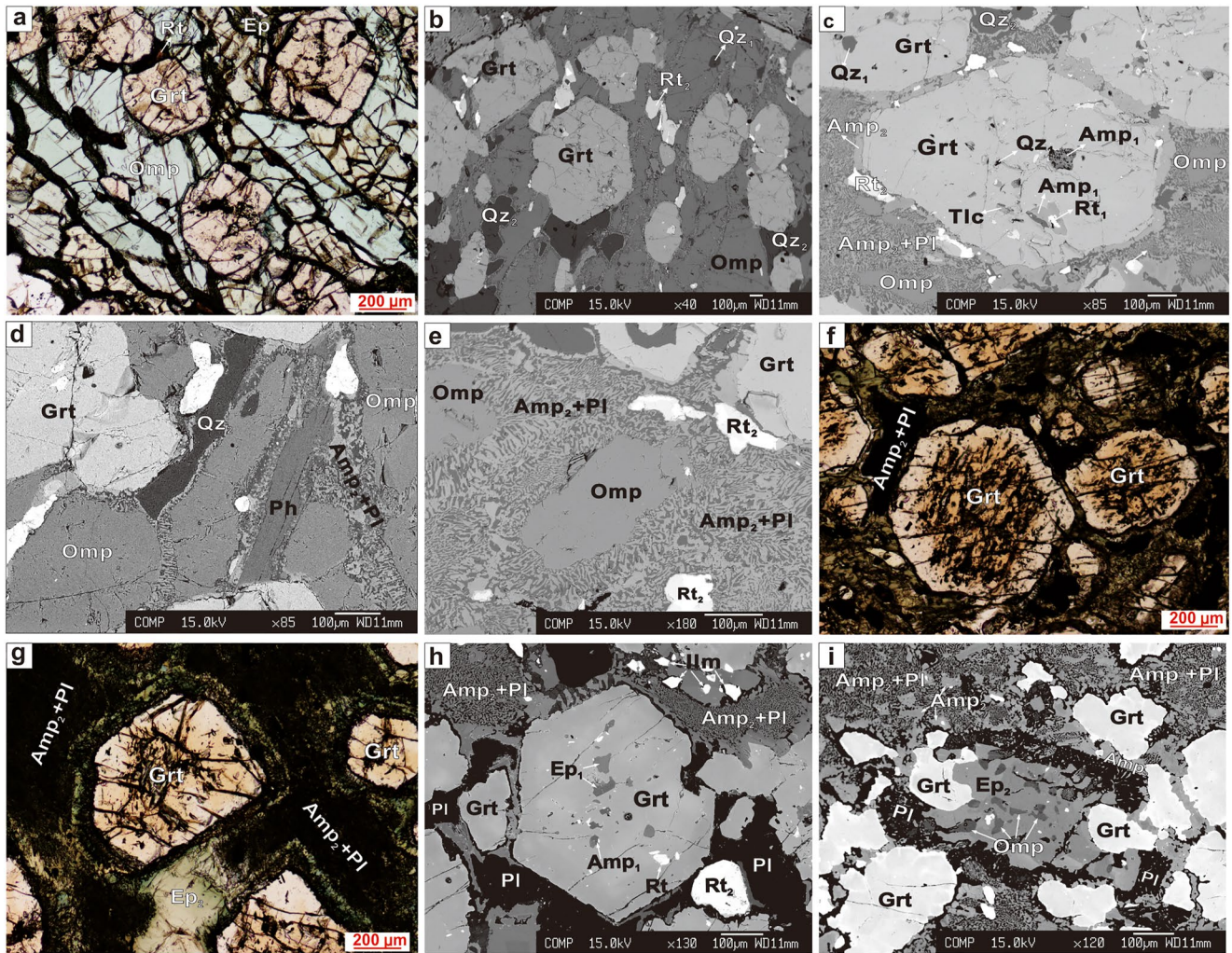


**Figure 4.** Microphotographs of the two new eclogites. (a) Photomicrographs of the eclogite with primary mineral assemblage of Grt + Omp, and accessory mineral of  $Rt_2$  (Urgamal). (b) BSE images of the eclogite with accessory minerals of  $Qz_2 + Rt_2$  distributing between Grt and Omp (Urgamal). (c) BSE images of Grt porphyroblast with mineral inclusions of  $Qz_1$ ,  $Rt_1$ , and  $Amp_1$  (Urgamal). (d) BSE images of symplectite of  $Amp_2 + Pl$  surrounding Omp (Urgamal). (e) BSE images of symplectite of  $Amp_3 + Pl_3$  surrounding Grt, Omp and  $Rt_2$  (Urgamal). (f) Photomicrographs of the retrogressed eclogite with symplectite of  $Amp_2 + Pl$  surrounding Grt (Tsengel). (g) Photomicrographs of Grt and Ep porphyroblast rimmed by  $Amp_2$  and Pl (Tsengel). (h) BSE image of Grt porphyroblast with mineral inclusions of Ep,  $Rt_1$ , and  $Amp_1$  (Tsengel). (i) BSE images of Omp occurring as inclusions in the Ep (Tsengel). Mineral abbreviations: Grt, garnet; Amp, amphibole; Omp, omphacite; Pl, plagioclase; Qz, quartz; Rt, rutile; Ep, epidote.

assemblage of  $Amp_1 + \text{epidote } (Ep_1) + Qz_1 + Rt_1$  found as inclusions within cores of garnet porphyroblast (Grt); a peak mineral assemblage of Omp (found as inclusions in  $Ep_2$ ) +  $Qz_2 + Rt_2$  plus the mantle domains of Grt; and a retrograde assemblage occurring as symplectites of  $Amp_2 + Pl \pm \text{Cpx}$ .

### 3. Analytical Methods

#### 3.1. Mineral Chemistry

Major element compositions of minerals were analyzed on a JEOL JXA-8100 Electron Probe with four wavelength dispersive spectrometers at the Institute of Geology and Geophysics, Chinese Academy of Sciences (IGGCAS), applying a 15-kV accelerating voltage and a 10-nA beam current. Count times were 10 s on peaks, and 5 s on each background. Natural minerals and synthetic oxides were used as standards. Minerals were analyzed for Na, Mg, Al, Si, K, Ca, Ti, Mn, Fe, Cr, and Zn. A program based on the ZAF procedure was used for data correction. Chemical compositions of representative minerals are presented in Tables S1 and S2 of Supporting Information S1.

### 3.2. Rutile Geochemistry

In situ analysis of major and trace element compositions of rutile was conducted by LA-ICP-MS method at Fluid Inclusion Laboratory (FIL), Key Laboratory of Mineral Resources, IGCCAS. A Coherent Geolas HD 193 nm ArF excimer laser-ablation system was used in conjunction with an Agilent 7900 ICP-MS instrument (Agilent Technologies, USA). Argon was used as the makeup gas and mixed with the carrier gas helium via a T-connector before entering into ICPMS. The laser spot diameter was 44  $\mu\text{m}$ , with the pulse rate of 5 Hz and energy density of 4 J/cm<sup>2</sup>. Each analysis involved 20 s of background acquisition and 50 s sample data acquisition, followed by 20 s flushing time. US National Institute of Standards and Technology (NIST) standard reference material (SRM) 610 was used as an external calibration standard with titanium (<sup>49</sup>Ti) as an internal standard for concentration calculation. The standard materials ARM-1 and BCR-2G were analyzed as unknown sample to check the data quality. The resulting data were processed based on the GLITTER program.

### 3.3. Whole-Rock Geochemistry

Whole-rock major and trace element compositions were determined at Hebei Regional Geological Survey Institute. Fresh samples were crushed and subsequently reduced to powder in an agate shatter box. Major oxides were analyzed in fused glass disks using an X-ray fluorescence spectrometer (XRF-1800). The precision is within  $\pm 2\%$  for the oxides greater than 0.5 wt.% and within  $\pm 5\%$  for the oxides greater than 0.1 wt.%. Whole-rock trace element analyses were performed by inductively coupled plasma mass spectrometry (ICP-MS). Samples were dissolved by a mixed acid of HNO<sub>3</sub> and HF in a Teflon vessel, and in high-pressure Teflon bombs at 120°C for 6 days. The solution was evaporated to incipient dryness, dissolved by concentrated HNO<sub>3</sub> and evaporated at 150°C to dispel the fluorides. The samples were diluted to about 80 g for analysis after re-dissolved in 30% HNO<sub>3</sub> overnight. The signal drift of the spectrometer was monitored by an internal standard rhodium solution. Analytical results for USGS standards indicated that the uncertainties during trace element analysis for most elements were within 5%. Whole-rock geochemistry of the two new eclogites are given in Tables S3 and S4 of Supporting Information S1.

### 3.4. Zircon U-Pb Geochronology

Zircon grains were separated from the crushed samples by conventional heavy liquid and magnetic separation technique. These grains were mounted with zircon standards in epoxy mount and polished to expose the zircon interiors. Transmitted and reflected light microphotographs and cathodoluminescence (CL) images obtained using a HITACHI S-3000N SEM were prepared to investigate internal texture and origin of the zircons.

Zircon U-Pb analysis by the SHRIMP secondary ionization mass spectrometry instrument was performed at the Beijing SHRIMP Center, Institute of Geology, Chinese Academy of Geosciences. Analytical procedures followed those of Williams (1998). The spot size of the ion beam was about 20  $\mu\text{m}$  and the intensity of the primary O<sub>2</sub><sup>-</sup> ion beam was 4–6 nA. Each spot was rastered for 3 min prior to analysis to remove surface common Pb. The analytical data were processed using the Excel-based programs SQUID 1.03 (Ludwig, 2001) and ISOPLOT 3.0 (Ludwig, 2003). Common Pb corrections used the measured <sup>204</sup>Pb and the <sup>204</sup>Pb-based methods of Compston et al. (1984). Weighted mean ages of individual samples are quoted at the 95% confidence level (2 $\sigma$ ). The analytical results are given in Tables S5 of Supporting Information S1.

Zircon U-Pb analysis by laser ablation inductively coupled plasma mass spectrometry (LA-ICP-MS) was performed at Beijing GeoAnalysis CO., LTD. An ablation diameter of 32  $\mu\text{m}$  was adopted during the analysis. Helium was used as a carrier gas to increase the transport efficiency of the ablated material. Zircon 91500 was used as the external standard to determine U-Pb age, whereas NIST610 as the external standard to calibrate the trace element contents of zircons. Zircon reference samples Plešovice (337 Ma; Sláma et al., 2008) and GJ-1 (609 Ma; Jackson et al., 2004) were analyzed to check accuracy. The analyses yielded weighted mean <sup>206</sup>Pb/<sup>238</sup>U ages of 604  $\pm$  6 Ma for GJ-1 and 337.5  $\pm$  1.5 Ma for Plešovice, which were in good agreement with the recommended ages of 609 Ma and 337 Ma, respectively. The analytical results are given in Table S6 of Supporting Information S1.

### 3.5. Radiogenic Isotope Analysis

The Sr and Nd isotope measurements were done at the Beijing Createch Testing Technology Co., Ltd. Isotopic compositions of Sr and Nd were determined using a Thermo Fisher Scientific Neptune Plus MC-ICP-MS.

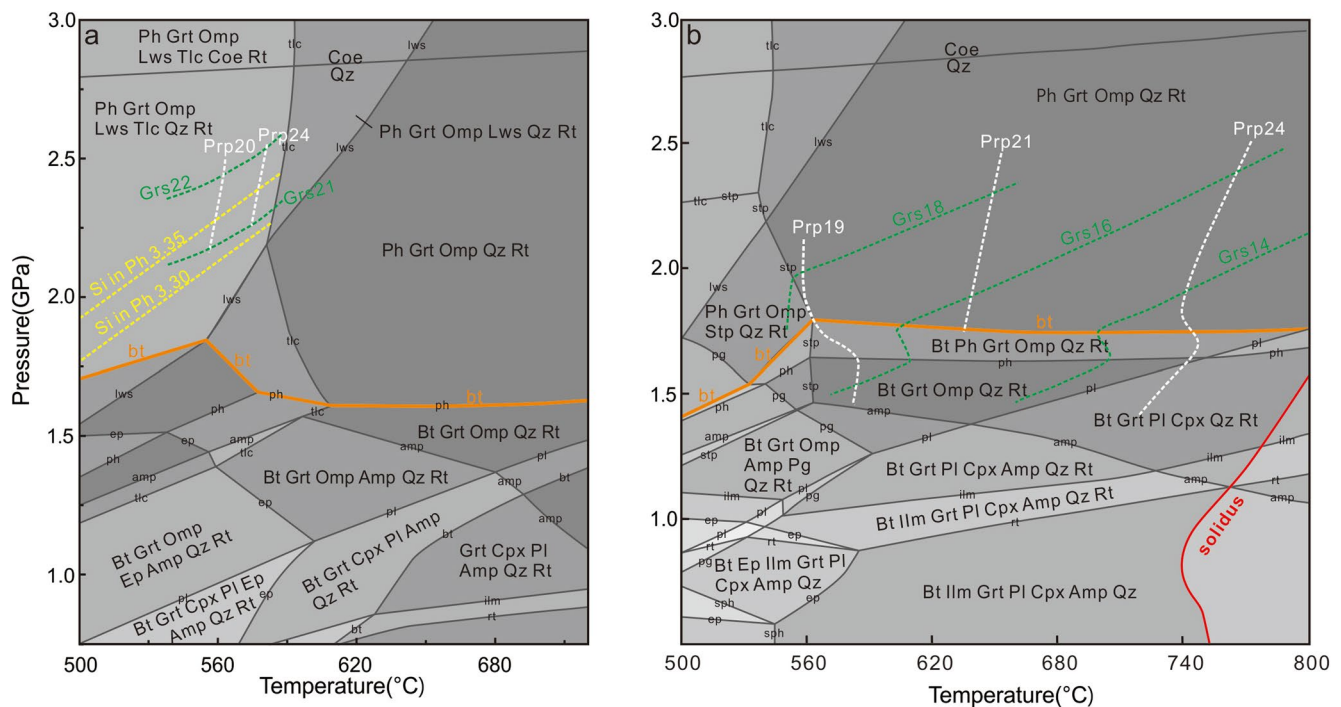


**Figure 5.** *P-T* pseudosections computed using measured bulk-rock composition for the two eclogites. (a) The Uргamal eclogite. (b) The Tsengel eclogite. The degree of freedom is represented by the gray values of the fields. The minerals on the field boundaries represent occurrence or disappearance of the minerals when cut across the boundaries. Prp and Grs isopleths of garnet, and Si-in phengite isopleths are represented by different lines as shown.

The  $^{87}\text{Sr}/^{86}\text{Sr}$  values were corrected for instrumental mass bias using the exponential fractionation law and assuming  $^{88}\text{Sr}/^{86}\text{Sr} = 8.375209$ .  $^{143}\text{Nd}/^{144}\text{Nd}$  ratios were corrected for instrumental mass bias using the exponential fractionation law and assuming  $^{146}\text{Nd}/^{144}\text{Nd} = 0.7219$ . The methods were modified from Y. Yang et al. (2010). Measurements of the international accepted Sr standard NBS-987 and Nd standard GSB-Nd in this study yielded  $^{87}\text{Sr}/^{86}\text{Sr} = 0.710248 \pm 19$  ( $2\sigma$ ) and  $^{143}\text{Nd}/^{144}\text{Nd} = 0.512195 \pm 5$  ( $2\sigma$ ), respectively. The analytical data are presented in Table S7 of Supporting Information S1.

## 4. Results

### 4.1. *P-T* Estimation

We used phase equilibria modeling (pseudosection) and conventional geothermobarometry to estimate metamorphic *P-T* conditions. Phase equilibria modeling was calculated in the MnNCKFMASHTO ( $\text{MnO-Na}_2\text{O-CaO-K}_2\text{O-FeO-MgO-Al}_2\text{O}_3\text{-SiO}_2\text{-H}_2\text{O-TiO}_2\text{-O}_2$ ) chemical system using the Perple\_X software (version 6.7.8; Connolly, 2005) and the internally consistent thermodynamic data set ds62 (Holland & Powell, 2011). Mineral solution models follow those used in Cao et al. (2019). Quartz,  $\text{H}_2\text{O}$ , and rutile were treated as pure phases. We used measured bulk-rock compositions of relatively homogenous parts of the eclogites. The FeO contents were determined by chemical titration. The  $\text{H}_2\text{O}$  contents were set to excess. The CaO contents associated with apatite were removed stoichiometrically on the basis of measured  $\text{P}_2\text{O}_5$  contents.

The *P-T* pseudosection calculated for the Uргamal eclogite is presented in Figure 5a. The inclusion assemblage enclosed within garnet cores likely reflects relics of a prograde metamorphism. The garnet mantle compositions suggest *P-T* conditions of  $\sim 560^\circ\text{C}$ ,  $\sim 2.2$  GPa in the field of Grt + Omp + Ph + Lws + Tlc + Rt + Qz (Figure 5a). The predicted field is generally consistent with the observed peak mineral assemblage, and thus records the peak pressure conditions. The absence of lawsonite in the sample is likely due to the lawsonite decomposition as a result of temperature increase and fluid infiltration during exhumation (Whitney & Davis, 2006). In addition, we plot measured Si-in phengite values on the phase diagrams and the results are broadly consistent with the *P-T* estimates (Figure 5a). Phase equilibrium modeling could give errors of 10% for pressure, and 5% for temperature

(Massonne, 2013; Palin et al., 2016). Besides, the garnet-omphacite-phengite geothermobarometer (Ravna, 2000; Waters & Martin, 1993, 1996) applied to the garnet mantle-core, omphacite core and phengite core yield  $P$ - $T$  conditions of 2.42–2.81 GPa and 516–603°C for the Urgamal eclogite, broadly consistent with phase equilibria modeling results for the peak pressure metamorphism, with uncertainties considered. Rutile in garnet and matrix rutile contains similar Zr contents, ranging from 157 to 244 ppm, and the Zr-in-rutile thermometry (Kohn, 2020) yields 651–690°C at 2.7 GPa, and 600–636°C at 1.7 GPa with an uncertainty of  $\pm 20$ –30°C. Amp-Pl geothermometer (Holland & Blundy, 1994) and Al-in-hornblende geobarometer (Anderson & Smith, 1995) constrain retrogression near 628°C and 0.76 GPa.

The  $P$ - $T$  pseudosection calculated for the Tsengel retrogressed eclogite is shown in Figure 5b. The inclusions enclosed within garnet cores likely record relics of a prograde metamorphism. The measured mineral compositions of the garnet mantle domains constrain  $P$ - $T$  conditions of 680–737°C and 1.76–2.10 GPa in the stability field of Grt + Omp + Ph + Rt + Qz (Figure 5b). The predicted field is generally consistent with our observed peak mineral assemblage with phengite interpreted to breakdown during the retrograde path. Biotite is not observed in the sample, so the pressure condition should be above 1.75 GPa (biotite-in line; Figure 5b). We note that the sample was extensively overprinted by latter amphibolite-facies metamorphism, as reflected by the high-Prp garnet rims. In addition, the Grt-Cpx Fe-Mg exchange geothermometer (Ravna, 2000) applied to the garnet mantle and omphacite core yields 615–662°C at 1.7 GPa and 634–683°C at 2.1 GPa for the Tsengel eclogite, broadly consistent with the phase equilibria modeling results, if uncertainties are considered. The Zr-in-rutile thermometry (Kohn, 2020) applied to matrix rutile (Zr contents ranging from 128 to 236 ppm) yields 603–655°C at 2.1 GPa, and 583–634°C at 1.7 GPa with an uncertainty of  $\pm 20$ –30°C. Amp-Pl geothermometer (Holland & Blundy, 1994) and Al-in-hornblende geobarometer (Anderson & Smith, 1995) constrain retrogression near 600°C and 1.0 GPa, likely reflect a late exhumation process.

#### 4.2. Whole-Rock Geochemistry

Two types of Urgamal eclogite samples were selected: (a) a fine-grained eclogite and (b) a coarse-grained retrogressed eclogite. The fine-grained eclogite samples have SiO<sub>2</sub> contents of 48.3–49.1 wt.%, Na<sub>2</sub>O of 1.9–2.7 wt.%, CaO of 9.7–10.2 wt.%, TiO<sub>2</sub> of 2.3–2.4 wt.%, Al<sub>2</sub>O<sub>3</sub> of 13.4–13.7 wt.%, Fe<sub>2</sub>O<sub>3</sub>T of 14.3–14.7 wt.%, MgO contents of 6.2–6.5 wt.%, and Mg# [= molar Mg/(Mg + Fe<sup>2+</sup>)] of 0.5. Compared with the fine-grained eclogites, the coarse-grained eclogite samples have similar SiO<sub>2</sub> (47.8–50.9 wt. %) and Na<sub>2</sub>O (2.6–3.1 wt. %), but relatively higher TiO<sub>2</sub> (2.9–3.1 wt. %) and Fe<sub>2</sub>O<sub>3</sub>T (15.5–16.0), and lower Al<sub>2</sub>O<sub>3</sub> (12.4–12.6 wt. %), CaO (8.0–9.0 wt. %) and MgO (4.1–4.4 wt. %; Mg# = 0.4) contents. The fine-grained eclogite samples show LREE enrichment [(La/Yb)<sub>N</sub> of 2.1–2.5] and no Eu anomalies (Eu/Eu\* = 0.96–0.97) (Figure 4a). The coarse-grained retrogressed eclogite samples have more pronounced LREE enrichment [(La/Yb)<sub>N</sub> of 5.8–7.0] and weak negative Eu anomalies (Eu/Eu\* = 0.82–0.89) (Figure 6a). In the primitive mantle-normalized spider diagram, the fine-grained eclogite samples are depleted in LILE (e.g., Rb, Ba, and Sr) and have moderate to strong negative anomalies in HFSE (e.g., Nb, Ta, Zr, and Hf), while the coarse-grained retrogressed eclogite samples have no HFSE negative anomaly (Figure 6b).

The Tsengel retrogressed eclogite samples have SiO<sub>2</sub> contents of 47.8–51.9 wt.%, Na<sub>2</sub>O of 2.1–3.2 wt.%, CaO of 8.2–10.6 wt.%, TiO<sub>2</sub> of 0.9–2.7 wt.%, Al<sub>2</sub>O<sub>3</sub> of 12.7–14.1 wt.%, Fe<sub>2</sub>O<sub>3</sub>T of 14.4–18.1 wt.%, and MgO of 4.2–7.6 wt. % (Mg# = 0.36–0.55). The samples show LREE enrichment [(La/Yb)<sub>N</sub> = 1.3–2.7 and (La/Sm)<sub>N</sub> = 1.0–1.9] and weak negative Eu anomalies (Eu/Eu\* = 0.83–0.94) (Figure 6c). In the primitive mantle normalized spider diagram, the retrogressed eclogite samples display negative Sr but positive Pb anomalies, and no HFSE (e.g., Nb, Ta, Zr, and Hf) negative anomalies (Figure 6d).

#### 4.3. Zircon U-Pb Geochronology

Eight samples were selected for Sensitive High Resolution Ion Microprobe (SHRIMP) and/or LA-ICP-MS U-Pb zircon dating. Zircon grains from the Urgamal retrogressed eclogite sample (WM-883) are euhedral to subhedral, and show patch-like structure without zoning (Figure 7a). Laser Raman spectroscopy reveals the presence of rare mineral inclusions of garnet and rutile (Figure 7b). Eighteen zircon grains were analyzed, and the measured U and Th concentrations vary from 55 to 845 ppm and from 1 to 7 ppm, respectively, with Th/U ratios between 0.003 and 0.021. Twenty analyses plot on and near concordia and yield a weighted mean <sup>206</sup>Pb/<sup>238</sup>U age of 522 ± 4 Ma (MSWD = 1.25; Figure 7c).

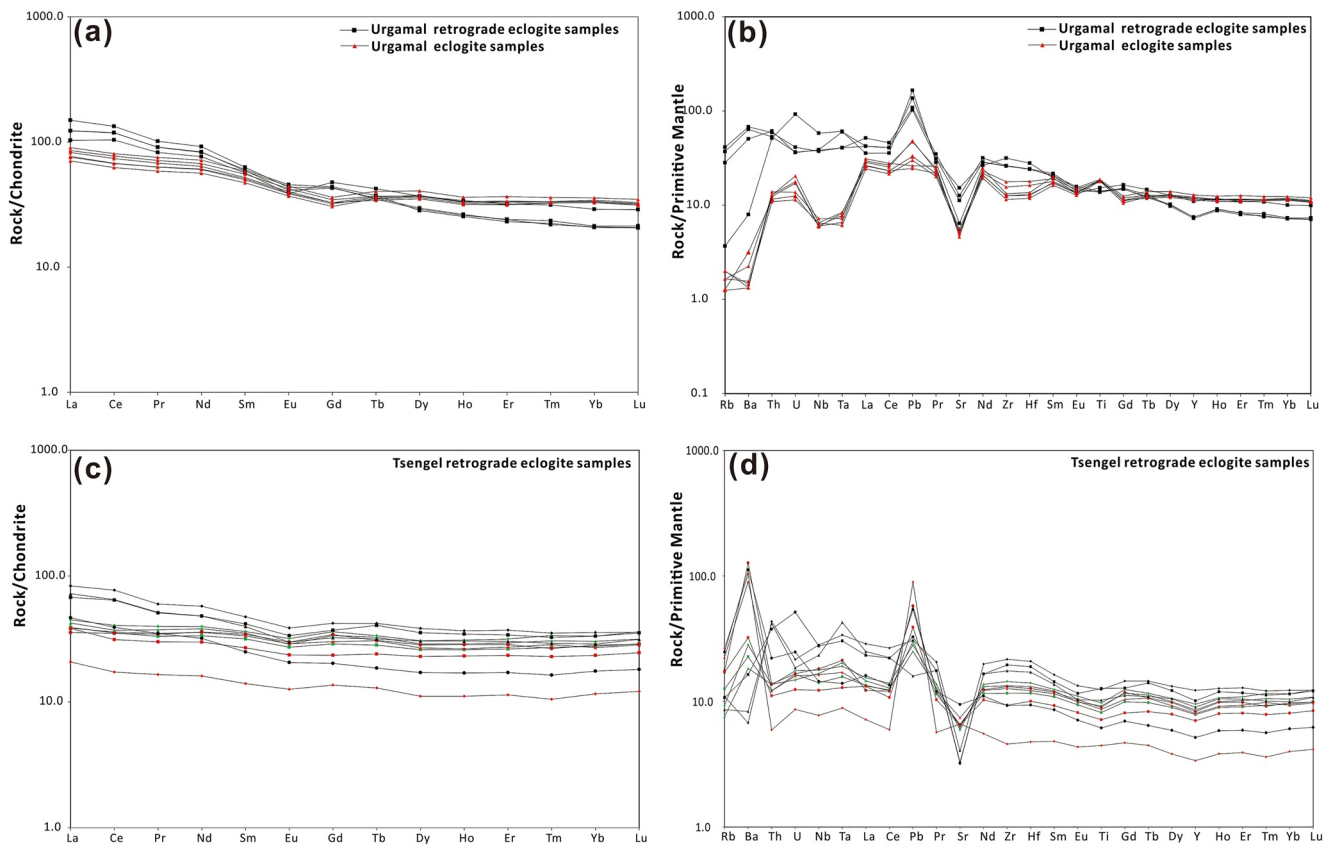


**Figure 6.** Geochemical plots of the two new eclogites. (a) Chondrite-normalized REE patterns for the Urgamal eclogite. (b) Primitive-mantle normalized diagrams for the Urgamal eclogite. (c) Chondrite-normalized REE patterns for the Tsengel eclogite. (d) Primitive-mantle normalized diagrams for the Tsengel eclogite. Normalizing values are from Sun and McDonough (1989) for both chondrite and primitive mantle.

Zircon grains from the granitic gneiss (WM-879) that encloses the Urgamal eclogite show oscillatory zoned cores with narrow high-luminescence (bright) rims (Figure 7a). Eighteen spot analyses from zircon cores with high Th/U ratios of 0.10–1.1 yield a concordia age of  $811 \pm 4$  Ma (MSWD = 1.20; Figure 7d). One zircon rim analysis yields an age of  $\sim 519$  Ma. Two spot analyses yielded older ages of  $\sim 1930$  and  $897$  Ma, and the remaining eight analyses yielded ages between 782 and 687 Ma.

Zircon grains from chlorite-biotite-quartz gneiss (sample WM-866), which was intercalated with the retrogressed eclogite, are euhedral to subhedral and 80–300  $\mu\text{m}$  long. They mostly display well-developed oscillatory zoning and very narrow unzoned rims (Figure 7a) too narrow to be analyzed. Except for one analysis with a very low Th/U ratio of 0.02, the remaining analyses have Th/U ratios ranging from 0.10 to 2.34, indicating an igneous origin for the analyzed zircon grains/domains. A total of 56 analyses yielded two prominent age peaks at  $\sim 802$  Ma and  $\sim 844$  Ma, respectively, and a number of Paleoproterozoic ages scattering between 1970 and 2477 Ma (Figures 7e and 7f).

Zircon grains from the quartz-feldspar gneiss (sample WM-872) that is intruded by retrogressed eclogite dykes are mostly sub-euhedral to rounded and are 100–250  $\mu\text{m}$  in diameter. Some of them display core-overgrowth structures (Figure 7a). The dark and unzoned overgrowth rims have very low Th/U ratios (0.007 and 0.014), and two analyses from these rims yielded  $^{206}\text{Pb}/^{238}\text{U}$  ages of  $506 \pm 5$  Ma and  $505 \pm 5$  Ma, respectively. By contrast, the zircon cores, which mostly show oscillatory zoning, have higher Th/U ratios of 0.15–2.27. Fifty-nine analyses of the zircon cores yielded three age peaks at  $\sim 1547$ , 2000, and 2458 Ma, respectively, and several older ages between 2610 and 3185 Ma (Figures 7g and 7h).

Zircons from the Tsengel retrogressed eclogite sample MS-59 are rounded or prismatic grains. CL images reveal that most zircons display core-overgrowth structures (Figure 8a). Ten analyses on the zircon cores plot on and around concordia and yield a weighted mean  $^{206}\text{Pb}/^{238}\text{U}$  age of  $853 \pm 16$  Ma (MSWD = 1.40; Figure 8c), with high

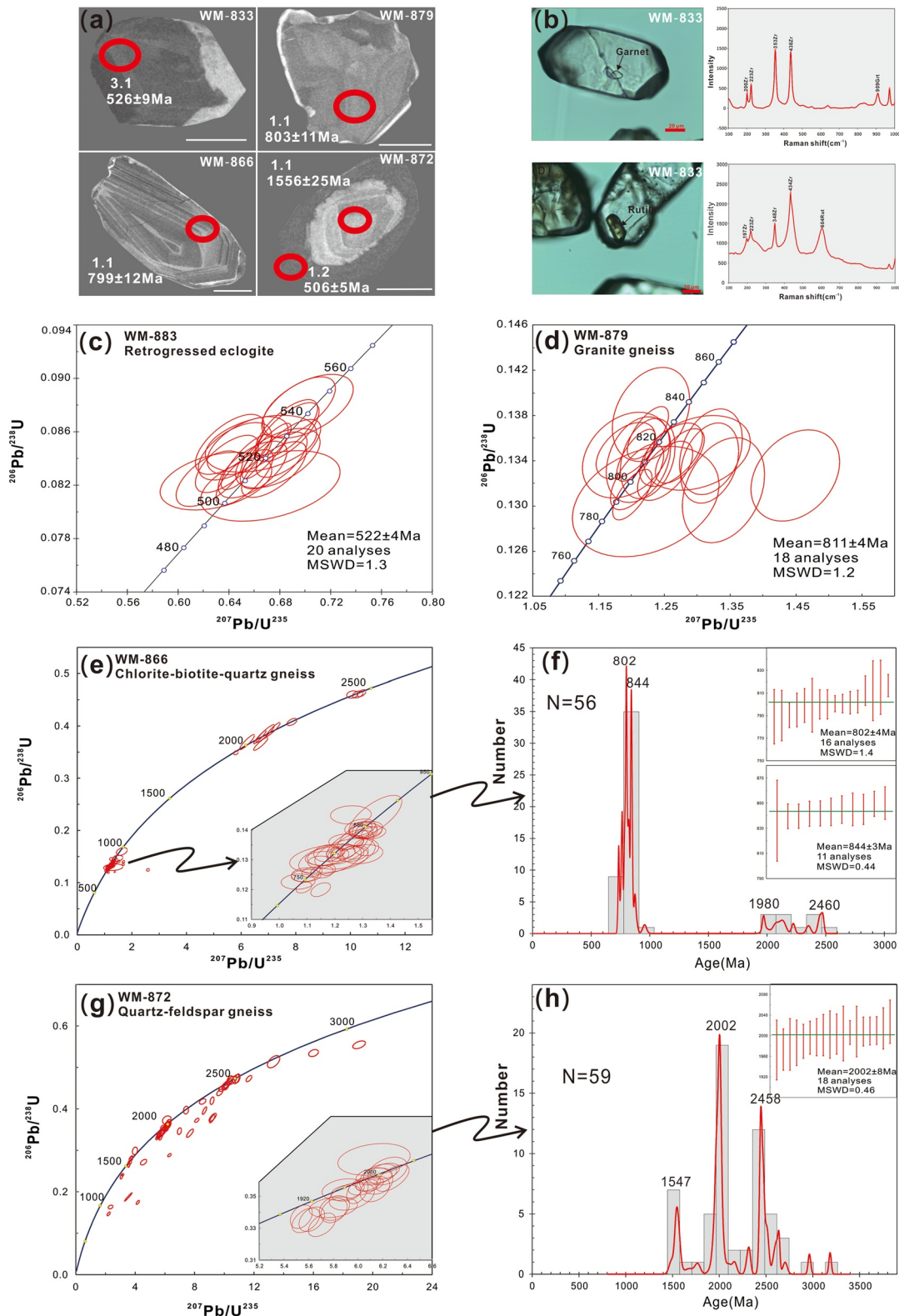


Figure 7.

Th/U ratios between 0.36 and 0.88. Eleven analyses on the overgrowth rims yielded a weighted mean  $^{206}\text{Pb}/^{238}\text{U}$  age of  $514 \pm 7$  Ma (MSWD = 2.20; Figure 8c) and Th/U ratios between 0.04 and 0.20. The remaining analyses yielded  $^{206}\text{Pb}/^{238}\text{U}$  ages scattering from 538 to 818 Ma.

Zircons from the Tsengel retrogressed eclogite sample MH-147 are subhedral and show patch-like structure without oscillatory zoning in CL images (Figure 8a). Laser Raman spectroscopy reveals the presence of mineral inclusions of garnet and rutile in the zircons (Figure 8b). Seventeen zircon grains from this sample were analyzed. The measured U and Th concentrations vary from 14 to 63 ppm and from 0.01 to 0.59 ppm, respectively, with low Th/U ratios (0.001–0.010). All of the 17 analyses plot on and near the concordia and yielded a weighted mean  $^{206}\text{Pb}/^{238}\text{U}$  age of  $524 \pm 6$  Ma (MSWD = 0.54; Figure 8d).

Zircons from the Tsengel retrogressed eclogite sample (MS-129) are similar in morphology and internal texture to those from sample MH-147 (Figure 8a). The measured U and Th concentrations vary from 103 to 420 ppm and from 2 to 14 ppm, respectively. Similarly, the low Th contents and Th/U ratios (0.02–0.04), together with the patchy texture in CL images, suggest a metamorphic origin for the zircon. Twenty-six analyses with low Th/U ratios of 0.02–0.04 yielded a concordia age of  $517 \pm 4$  Ma (MSWD = 0.37; Figure 8e).

Zircons from a migmatite gneiss sample (MS-99), which hosts the Tsengel retrogressed eclogite, are euhedral to subhedral prisms that are 100–300  $\mu\text{m}$  long (Figure 8a). Most zircons show well-developed oscillatory zoning. Thirty-one zircon grains were chosen for analysis. The measured U and Th concentrations vary from 35 to 3,410 ppm and from 9 to 9,300 ppm, respectively, with Th/U ratios between 0.11 and 2.73. All the analyses plot on and near the concordia, of which twenty-two analyses yielded a weighted mean  $^{206}\text{Pb}/^{238}\text{U}$  age of  $517 \pm 4$  Ma (MSWD = 0.37; Figure 8f). Five spots analyses yield a weighted mean  $^{206}\text{Pb}/^{238}\text{U}$  age of  $807 \pm 12$  Ma (MSWD = 0.37; Figure 8f). Two spots analysis yield older  $^{206}\text{Pb}/^{238}\text{U}$  age of 882 Ma and 894 Ma, and the remaining two analyses yielded  $^{206}\text{Pb}/^{238}\text{U}$  ages of 596 Ma and 547 Ma.

#### 4.4. Sr-Nd Isotope Compositions

Eleven eclogite samples were analyzed for Sr-Nd isotopes, and the analytical data are presented Figure 9. Though direct geochronological data on the protolith age of the Urgamal eclogite are unavailable, this age should be older than the metamorphic age of  $\sim 522$  Ma, and younger than the suggested crystallization age of  $\sim 811$  Ma for the eclogite-hosting granitic gneisses. If the initial isotopic ratios are calculated based on the age of 522 Ma, the fine-grained eclogite samples have radiogenic  $\epsilon_{\text{Nd}(t)}$  values of  $-3.3$  to  $-2.9$ , and moderate ( $^{87}\text{Sr}/^{86}\text{Sr}$ )<sub>i</sub> ratios (0.7083–0.7085). The three coarse-grained retrogressed eclogite samples have  $\epsilon_{\text{Nd}(t)}$  values of  $-7.6$  to  $-8.1$ , and ( $^{87}\text{Sr}/^{86}\text{Sr}$ )<sub>i</sub> ratios of 0.7079–0.7095. If the initial isotopic ratios were calculated based on the age of 811 Ma, the fine-grained eclogite samples have radiogenic  $\epsilon_{\text{Nd}(t)}$  values of  $-2.4$  to  $-1.5$ , and ( $^{87}\text{Sr}/^{86}\text{Sr}$ )<sub>i</sub> ratios (0.7080–0.7084). The three coarse-grained retrogressed eclogite samples have radiogenic  $\epsilon_{\text{Nd}(t)}$  values of  $-6.2$  to  $-5.3$ , and ( $^{87}\text{Sr}/^{86}\text{Sr}$ )<sub>i</sub> ratios of 0.7067–0.7093. The initial isotopic ratios of the Tsengel eclogite were calculated based on the measured SHRIMP U-Pb age of 849 Ma. The Tsengel eclogite samples have positive  $\epsilon_{\text{Nd}(t)}$  values of 1.2–4.8, and moderate ( $^{87}\text{Sr}/^{86}\text{Sr}$ )<sub>i</sub> ratios of 0.7033–0.7052.

## 5. Discussion

### 5.1. Metamorphic and Protolith Ages of the Eclogites and Their Country Rocks

The zircons from the Urgamal retrogressed eclogite (sample WM-883) have low Th concentrations and Th/U values (0.003–0.021), together with the garnet inclusions in zircons, suggesting a metamorphic origin (Hoskin & Black, 2000; Hoskin & Schaltegger, 2003). Thus, the weighted mean age of  $522 \pm 4$  Ma is interpreted as the age of eclogite-facies metamorphism of the Urgamal retrogressed eclogite. The zircon cores from the granitic gneiss show well-developed oscillatory zoning and high Th/U values with similar features of igneous origin (Hoskin & Black, 2000), and yielded a weighted mean age of  $811 \pm 4$  Ma, possibly representing the age of emplacement

**Figure 7.** CL images of zircons, Laser Raman spectroscopy of inclusions in zircons and U-Pb concordia diagrams of the Urgamal eclogite and its host rocks. (a) Red circles represent sites of analytical spots, and the numbers around the circles are the spot numbers and ages (with  $2\sigma$  error). The scale bar is 50  $\mu\text{m}$ . (b) Laser Raman spectroscopy of garnet and rutile inclusions in the analyzed zircons. (c) Sample WM-883 from the retrogressed eclogite. (d) Sample WM-879 from the granite gneiss entrapping the retrogressed eclogite. (e and f) Detrital zircon U-Pb concordia and relative probability diagrams for sample WM-866 chlorite-biotite-quartz gneiss. (g and h) Detrital zircon U-Pb concordia and relative probability diagrams for sample WM-872 quartz-feldspar gneiss.

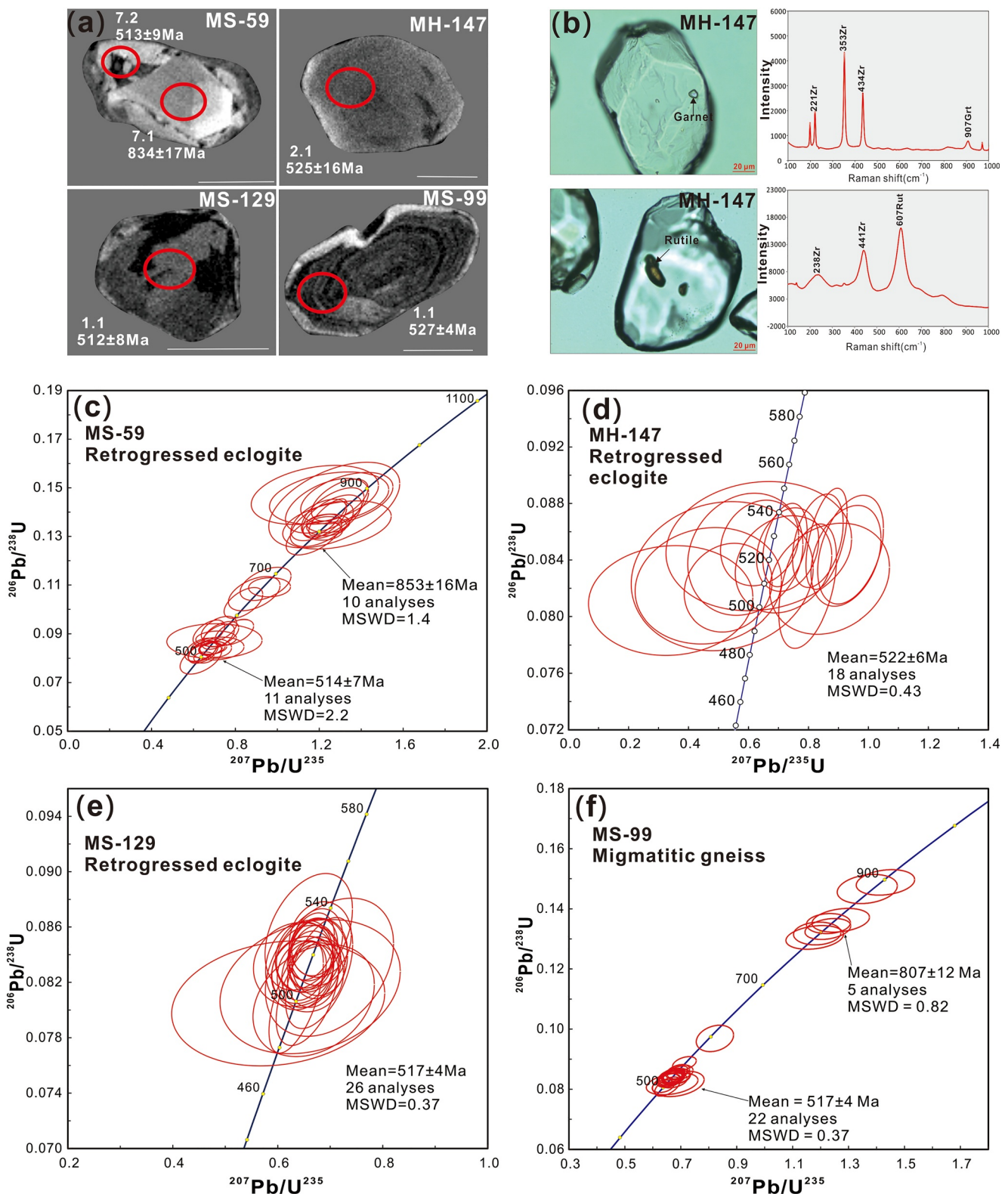


**Figure 8.** CL images of zircons, Laser Raman spectroscopy of inclusions in zircons and U-Pb concordia diagrams of the Tsengel eclogite and its host rocks. (a) Red circles represent sites of analytical spots, and the numbers around the circles are the spot numbers and ages (with  $2\sigma$  error). The scale bar is 50  $\mu\text{m}$ . (b) Laser Raman spectroscopy of garnet and rutile inclusions in the analyzed zircons. (c) Sample MS-59 from the retrogressed eclogite. (d) Sample MH-147 from retrogressed eclogite. (e) Sample MS-129 from retrogressed eclogite. (f) Sample MS-99 from migmatitic gneiss.

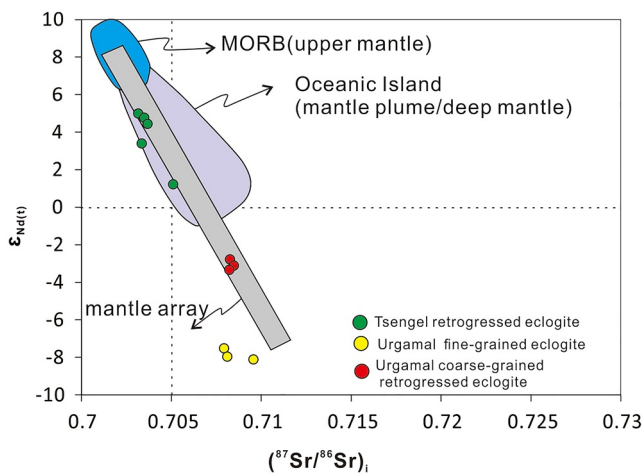


**Figure 9.**  $\epsilon_{Nd(t)}$  versus  $(^{87}Sr/^{86}Sr)_t$  diagram for the eclogites. Reference data sources: MORB (Rollinson, 1993; Sun & McDonough, 1989), OIB (Vervoort et al., 1999), mantle array (Wilson, 1989).

of the granite. The  $\sim 519$  Ma from the zircon rim possibly represents the metamorphic age of the granitic gneiss, which is within error of the metamorphic age of the eclogite ( $\sim 522$  Ma). The zircons with older ages ( $\sim 1930$  and  $897$  Ma) possibly record zircon inheritance during the intrusion of the protolith of the granitic gneiss. The large age range of other analyses ( $782$ – $687$  Ma) may reflect incomplete recrystallization of cores during metamorphism and/or the analytical spots straddling on the zircon cores and overgrowth rims.

The two paragneiss samples (WM-866 and WM-872) enclosing the Urgamal eclogite show a wide distribution of detrital zircon core ages. The data show three dominant populations of  $2700$ – $2440$  Ma (peak at  $\sim 2500$  Ma),  $2300$ – $1900$  Ma (peak at  $\sim 2000$  Ma), and  $880$ – $730$  Ma (peaks at  $\sim 800$  and  $840$  Ma), and subordinate population of  $\sim 1700$ – $1400$  Ma. These populations are compatible with those of the Neoproterozoic rocks in the Zavkhan microcontinent (Bold, Crowley, et al., 2016; Bold, Smith, et al., 2016) (Figure 10). Consequently, we interpret the detrital zircon grains of the paragneiss were derived from the Zavkhan microcontinent, with the Paleoproterozoic detrital zircon grains likely from the crystalline basement rocks of the microcontinent and those with prominent peak ages of  $850$ – $780$  Ma from the coeval arc-volcanic and volcanoclastic rocks ( $\sim 811$ – $787$  Ma) (Bold, Crowley, et al., 2016; Bold, Smith, et al., 2016; Levashova et al., 2010). The zircon

rims from the quartz-feldspar gneiss (sample WM-872) have very low Th/U ratios (0.007 and 0.014) and yielded an age of  $\sim 505$  Ma, which is interpreted as the metamorphic age of the quartz-feldspar gneiss.

Although the zircon grains are slightly different in morphology and internal structures, the three dated Tsengel retrogressed eclogite samples (MS-59, MH-147, MS-129) yielded similar ages of  $514 \pm 7$ ,  $522 \pm 6$ , and  $517 \pm 4$  Ma, respectively. We interpret these ages to record the time of eclogite-facies metamorphism of the Tsengel retrogressed eclogite. Supporting evidence for this interpretation includes: (a) the zircon grains or zircon domains giving these ages are either homogeneous rounded grains (samples MH-147 and MS-129) or zircon overgrowth rims (sample MS-59) that show no oscillatory zoning in CL images and a morphology typical of zircons with metamorphic origin (e.g., Hoskin & Black, 2000); (b) the analyzed domains giving these ages have very low Th contents (0.01–141 ppm) and Th/U ratios (0.001–0.2), values characteristic of metamorphic zircons (Hoskin & Black, 2000; Hoskin & Schaltegger, 2003); (c) Laser Raman spectroscopy reveals the presence of mineral inclusions of garnet and rutile in the metamorphic zircons of sample MH-147.

Zircons in the migmatite gneiss (sample MS-99) which hosts the Tsengel retrogressed eclogite have a weighted mean age of  $517 \pm 4$  Ma. These grains have high Th/U ratios ( $>0.1$ ) and well-developed oscillatory zoning, which suggest a magmatic origin (Hoskin & Schaltegger, 2003). We therefore, interpreted the age of  $\sim 517$  Ma as a migmatization time. Importantly, this age ( $517 \pm 4$  Ma) is compatible with the metamorphic age ( $522$ – $514$  Ma) of the retrogressed eclogite, implying that the migmatization was coeval with the HP metamorphism, and thus suggesting a tectonic relation between them. We infer that the partial melting responsible for the migmatitic melt was possibly triggered by the dehydration by breakdown of hydrous minerals during the exhumation of the subducted HP rocks (e.g., Cao et al., 2019; Zheng et al., 2011).

The zircon cores that are rimmed by metamorphic overgrowths (sample MS-59) yielded a weighted mean age  $\sim 853$  Ma. Because the zircon cores giving the age are characterized by well-developed oscillatory zoning in CL images and by having high Th/U ratios (0.36–0.88), typical features of magmatic origin (Hoskin & Black, 2000), we interpreted this age to date the crystallization time of the protolith of the Tsengel eclogite, that is, the protolith formed during the early Neoproterozoic time. The scattering of other zircon ages ( $538$ – $818$  Ma) probably reflect incomplete recrystallization of cores during metamorphism and/or the analytical spots straddling on the zircon cores and overgrowth rims.

## 5.2. Protoliths and Tectonic Settings of the Eclogites

The two new eclogites have low silica contents, relatively high  $Fe_2O_3$  and MgO contents, and very weak negative Eu anomalies, indicating that they are likely metamorphosed from mafic protoliths. However, the low Mg# values

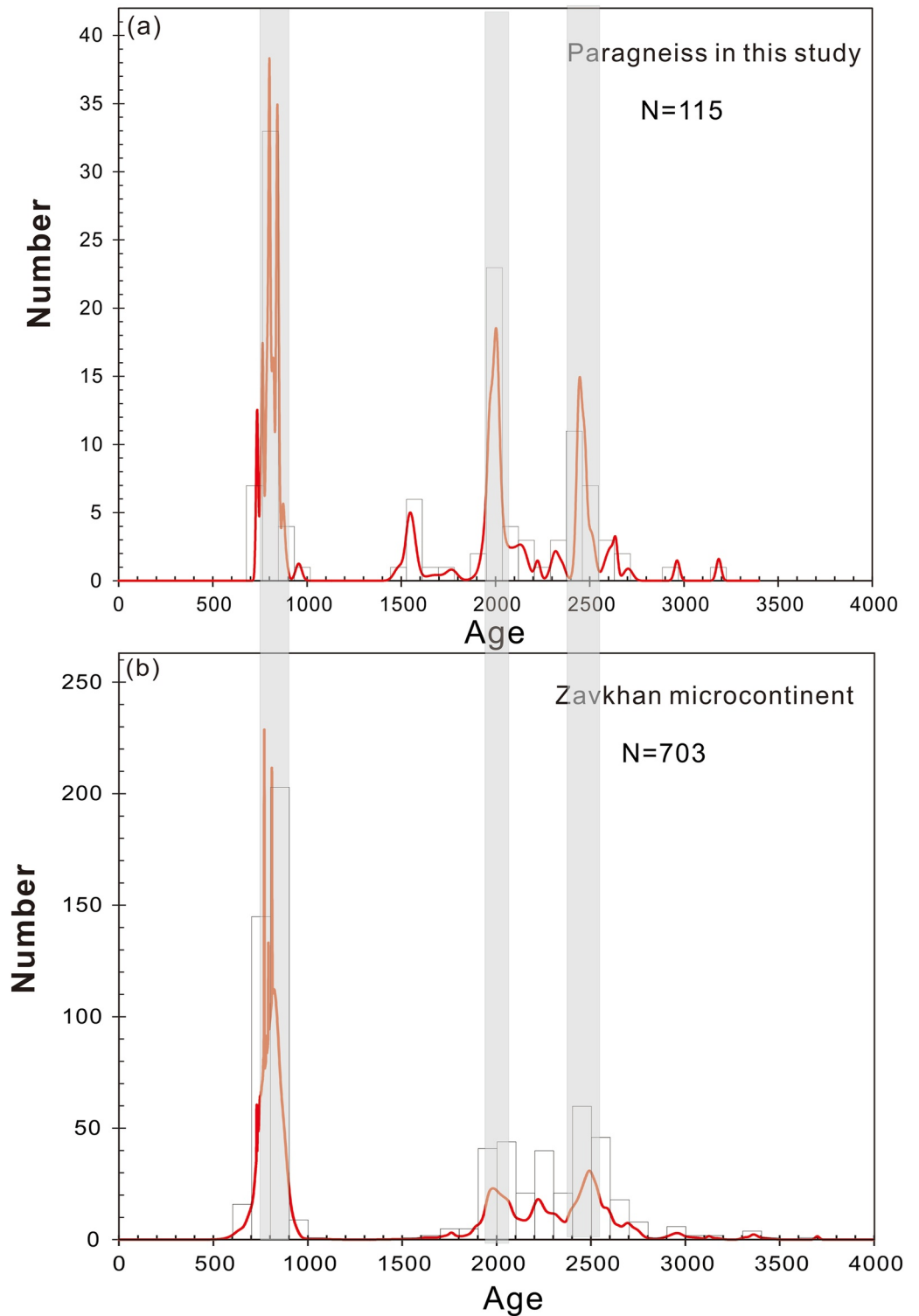


**Figure 10.** Comparison of Precambrian zircon populations of the paragneiss associated with the Urgamal eclogite and Zavkhan microcontinent. Precambrian zircon ages of Zavkhan microcontinent are compiled from literature Bold, Crowley, et al. (2016) and Bold, Smith, et al. (2016).

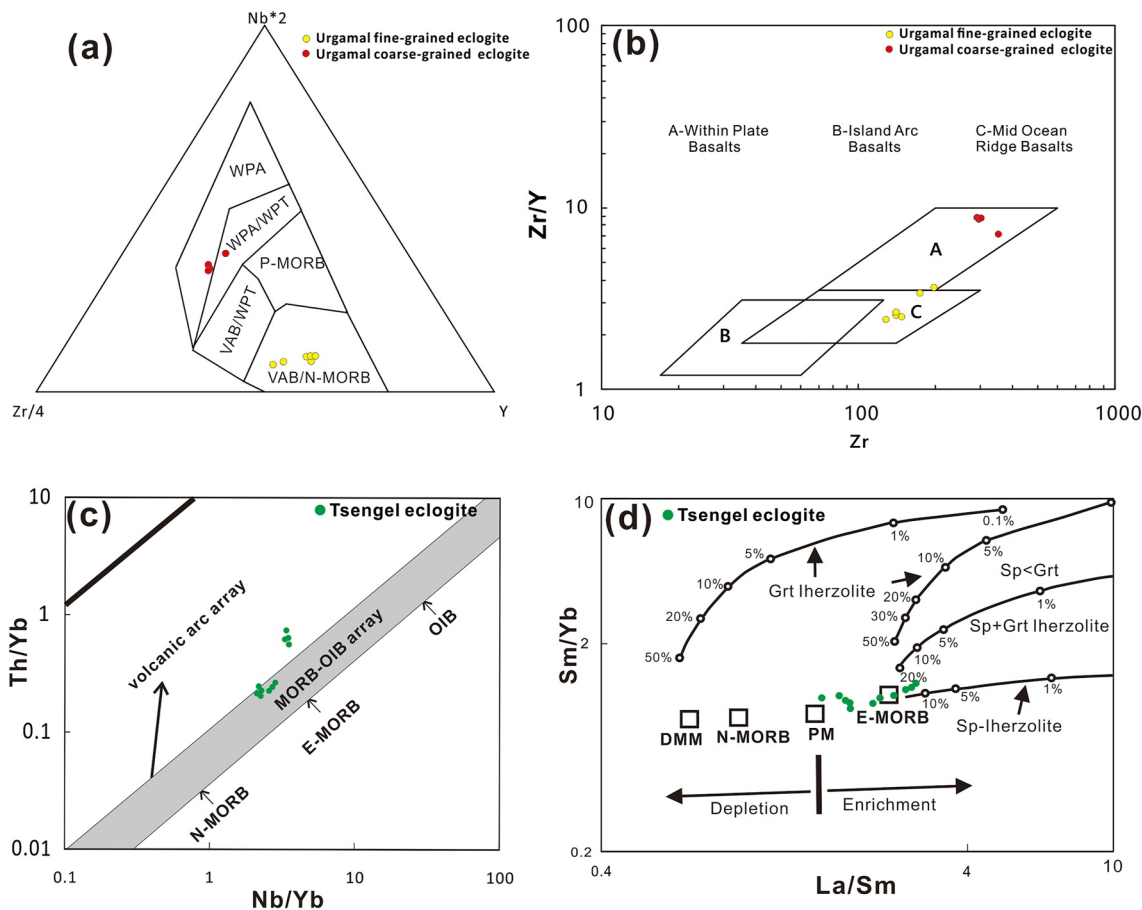


**Figure 11.** Tectonic discriminant diagrams for the two eclogites. (a) Nb-Zr-Y diagram for the Urgamal eclogite (Meschede, 1986). (b) Zr/Y versus Zr diagram for the Urgamal eclogite (Pearce & Norry, 1979). (c) Th/Yb-Nb/Yb diagram for the Tsengel eclogite (Pearce, 2008); (d) La/Sm and Sm/Yb diagram for the Tsengel eclogite (Aldanmaz et al., 2000). MORB, normal mid-ocean ridge basalt; WPA, within plate alkaline basalt; WPT, within plate tholeiite; IAB, island arc basalt.

(0.36–0.55) of the eclogites reflect the evolved nature of the precursor mafic rocks. The Urgamal fine-grained eclogite and coarse-grained retrogressed eclogite show different major elements, trace element and Sr-Nd isotope characteristics, demonstrating that they have different protoliths. The fine-grained eclogite shows LREE enrichment and Nb-Ta and Zr-Hf negative anomalies, which may have been derived from either contamination by continental crust material or subduction processes (e.g., Bonin, 2004; Xia & Li, 2019). However, their very low Th/Ce (0.02–0.03) and Th/La (0.05–0.06) ratios rule out significant crustal contamination. The lack of correlation between  $\epsilon_{Nd(t)}$  and  $SiO_2$  further supports this interpretation. The arc signatures and the negative  $\epsilon_{Nd(t)}$  values for the fine-grained eclogite suggest that its basaltic protolith was likely formed from partial melting of an enriched continent lithospheric mantle that might have been affected by some subduction events (e.g., Bonin, 2004). The coarse-grained retrogressed eclogite samples show OIB-like geochemical features, such as LREE enrichment, no HFSE negative anomalies, and more negative  $\epsilon_{Nd(t)}$  values, indicating that the protolith was generated by melting an enriched continent lithospheric mantle that might have not been influenced by subduction processes. It is noted that the lack of detrital zircon grains with ages between 740 and 570 Ma, along with the Neoproterozoic stratigraphic architecture, implies the development of a rifted passive continental margin during this period (Bold, Smith, et al., 2016). Thus, we suggest that the quartz-feldspar gneiss with the youngest detrital-zircon age of 1487 Ma probably represents the age of microcontinent basement, and that the chlorite-biotite-quartz gneiss sample having the youngest age of  $\sim 730$  Ma represents the Neoproterozoic rift-related metasedimentary rocks.

In both the Nb-Zr-Y and the Zr/Y versus Zr diagrams, all the coarse-grained retrogressed eclogite samples plot in the Within Plate Basalt (WPA) field whereas the fine-grained eclogite samples plot in the Volcanic Arc Basalt/N-MORB field and MORB field, respectively (Figures 11a and 11b). Their occurrences as layers intercalated with terrigenous sedimentary rocks and as dyke-like bodies within the granitic gneisses demonstrate these eclogites

were likely transformed from the basalts/diabase in a continental rift setting. The protolith of the Urgamal eclogite must be younger than the ~811 Ma granitic gneiss it was intruded into. It is plausible that this protolith formed 770–725 Ma ago—a period during which the region saw the widespread intrusion of rift-related alkaline granites and mafic intrusions of the Irkutsk LIP, and accumulation of Neoproterozoic passive margin clastic-carbonate sequences (e.g., Bold, Crowley, et al., 2016; Ernst et al., 2016; Gladkochub et al., 2019).

The Tsengel retrogressed eclogite samples show E-MORB-like geochemical feature with LREE enrichment but no HFSE negative anomalies, indicating the mantle source of the precursor basalt had not been contaminated by either subduction or crustal material prior to the basaltic magmatism. This conclusion is supported by the Th/Y versus Nb/Y and Sm/Yb versus La/Sm diagrams, in which all the retrogressed eclogite samples plot in and/or near the E-MORB field (Figures 11c and 11d). Combining their positive  $\varepsilon_{\text{Nd}(t)}$  and age data, we suggest that the Tsengel retrogressed eclogite was metamorphized from early Neoproterozoic oceanic crust, which was possibly generated from mantle plume-ridge interaction or by melting of a mantle enriched by mixing with metasomatized mantle (e.g., Gale et al., 2013). The Tsengel retrogressed eclogite mainly occurs as lenses or blocks in the mica-quartz schist, gneiss, and marble, typical of block-in-matrix structure of mélanges (e.g., Wakabayashi, 2017). Therefore, we interpret the retrogressed eclogite as relics of the OPS (Ocean Plate Stratigraphy), and the associated mica-quartz schist, gneiss and marble as represent trench turbidites and/or sediments deposited on subducted ocean crust and seamounts.

### 5.3. >1,000 km High-Pressure Metamorphic Belt and Its Tectonic Implications

There are three occurrences of Cambrian eclogite/retrogressed eclogite in West Mongolia (Štípská et al., 2010; this study). Among them, the Tsakhir Uul eclogite (~536–547 Ma; Štípská et al., 2010) is located along the contact of the Lake zone arc belt and the Baydrag microcontinent. The Tsakhir Uul eclogite boudins and lenses occur within the orthogneisses and metapelites of Alag Khadny crystalline complex, which show similar compositional characteristics with the ~948–941 Ma high-grade rocks of the Zamtyr Nuruu crystalline complex as part of the Baydrag microcontinent basement (Buriánek et al., 2017; Skuzovatov, 2021; Skuzovatov et al., 2018). Geochemical data suggest that the protoliths of the Tsakhir Uul eclogite have transitional mid-ocean ridge basalt (T-MORB) characteristics and probably originated from a heterogeneously enriched mantle source during Neoproterozoic continental rifting (Skuzovatov et al., 2018). Regardless of the difference in protolith, both newly discovered eclogites occur between the microcontinents and Ediacaran-Cambrian island arc belts (Figures 1 and 12), and were subducted to eclogite facies along a similar *P-T* path and at the same time (~520 Ma). Combined with the Tsakhir Uul continent-type eclogite, these three eclogites appear to form a Cambrian HP metamorphic belt >1,000 km in length along the margins of the Mongolian microcontinents (Figure 12). This belt can be traced beyond the location of these eclogites in the tract of the Mongolian Orocline (Figure 12), which is one of the two tightly curved oroclines of the CAO (Xiao et al., 2015). The Mongolian orocline shows a convex-to-the-west U-geometry defined by Permian-Triassic magmatic belts (Middle Gobi and Selenge magmatic belt) and microcontinental ribbons (Tarvagatay, Tuva-Mongolia, Zavkhan-Baydrag, and Idermeg microcontinents) (P. Li et al., 2022). Paleomagnetic, structural and geochronological data show that the Mongolian orocline resulted from bending in the Permo-Jurassic of an originally linear orogen (Edel et al., 2014; Lehmann et al., 2010). The original occurrences of these eclogites were roughly linear during Cambrian, and the Permian-Jurassic oroclinal bending rotated them to their actual position around the hinge zone of the Mongolian orocline (Figures 1 and 12). The correlation is supported by the Ediacaran-Cambrian arc belt bordering the newly-discovered HP belt, which can be traced from the Lake zone northward into Tannuola-Khamsara zone (Wilhem et al., 2012; Windley et al., 2007), probably extending to the Dzhida and Olkhon zone (Janoušek et al., 2018; Figure 12).

The recognition of this laterally extensive Cambrian HP metamorphic belt permits an updated tectonic model for the CAO during the Neoproterozoic to Cambrian (Figure 13). Rodinia was a Meso-Neoproterozoic supercontinent surrounded by the Pan-Rodinia Mirovoi Ocean (e.g., Z. X. Li et al., 2008; Zhao et al., 2018). The ~1020 Ma Dunzhungur ophiolite of East Sayan (Khain et al., 2002), ~972–892 Ma Shamanka ophiolite suite in the Transbaikalian sector (Gordienko et al., 2010) and the ~973 Ma Erdene Uul ophiolite in West Mongolia (Buriánek et al., 2017) probably represents fragments of the Mirovoi Ocean or marine basins within it (Buriánek et al., 2017; Kovach et al., 2021). The ~940 Ma orthogneisses from the Zamtyr Nuruu Complex along the southern margin of the Baydrag microcontinent (Buriánek et al., 2017), ~800–780 Ma arc-related complex (Zavkhan Formation, Kholbonur Complex and Sarkhoy volcanic sequences) along the west margin of the Zavkhan micro-

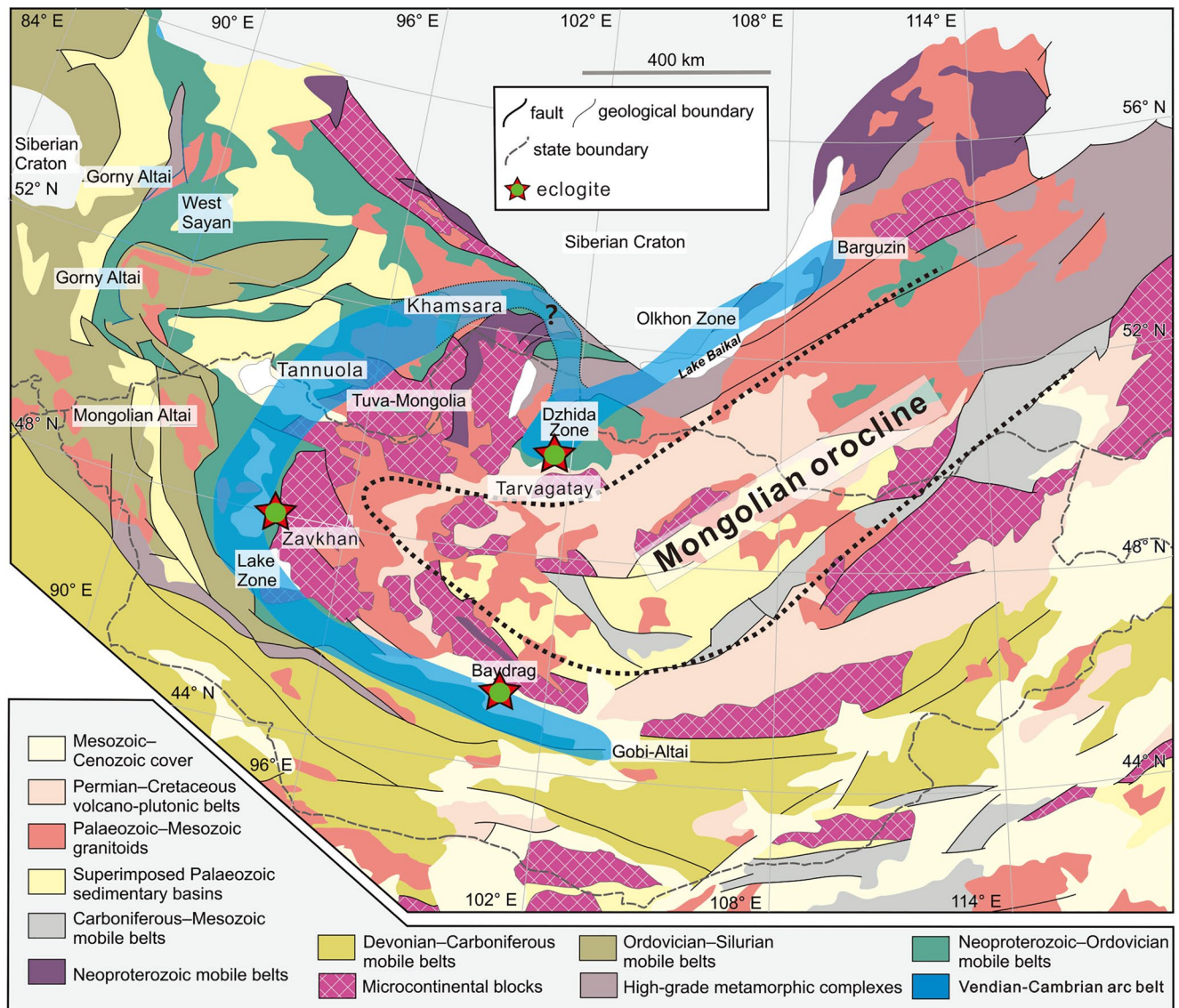


**Figure 12.** Simplified tectonic map of the central CAOB (modified from Parfenov et al. (2003) and Janoušek et al. (2018)) to show the linkage of the Cambrian HP eclogites and the bordering Ediacaran-Cambrian arc.

continent and Tuva-Mongolia microcontinent (Bold, Crowley, et al., 2016; Kovach et al., 2021; Kuzmichev & Larionov, 2011; Kuzmichev et al., 2005), ~835–824 arc-related magmatic rocks in the Baikal-Muya belt (Rytsk et al., 2001), ~937–891 Ma magmatism in the Bureya Block (H. Yang et al., 2020) are each interpreted to be the result of the consumption of the Mirovoi Ocean. We interpret the protoliths of the Tsengel retrogressed eclogite (~849 Ma) and associated formations as part of the early Neoproterozoic subduction-accretion complex that developed along the active continental margins of Rodinia (e.g., Kovach et al., 2021; Zhao & Zhou, 2008; Zhao et al., 2018) (Figure 13a).

The breakup of Rodinia occurred mainly between 750 and 600 Ma, leading to the opening of the Proto-Pacific, Iapetus and Paleo-Asian Ocean (e.g., Cawood et al., 2007; Z. X. Li et al., 2008; Zhao et al., 2018). The ~740–725 Ma mafic intrusions within Sayan and Baikal segments (the Irkutsk LIP) are suggested to be associated with the opening of the Palaeo-Asian Ocean (e.g., Ernst et al., 2016; Gladkochub et al., 2019). The protoliths of the Urgamal eclogite and the Tsakhir Uul eclogite were formed in a continental-rift environment probably related to this phase of supercontinent breakup which caused the CAOB microcontinents to detach from the Tarim or South China domains of Rodinia (e.g., Levashova et al., 2011; Figure 13b). This event broadly coincides with the

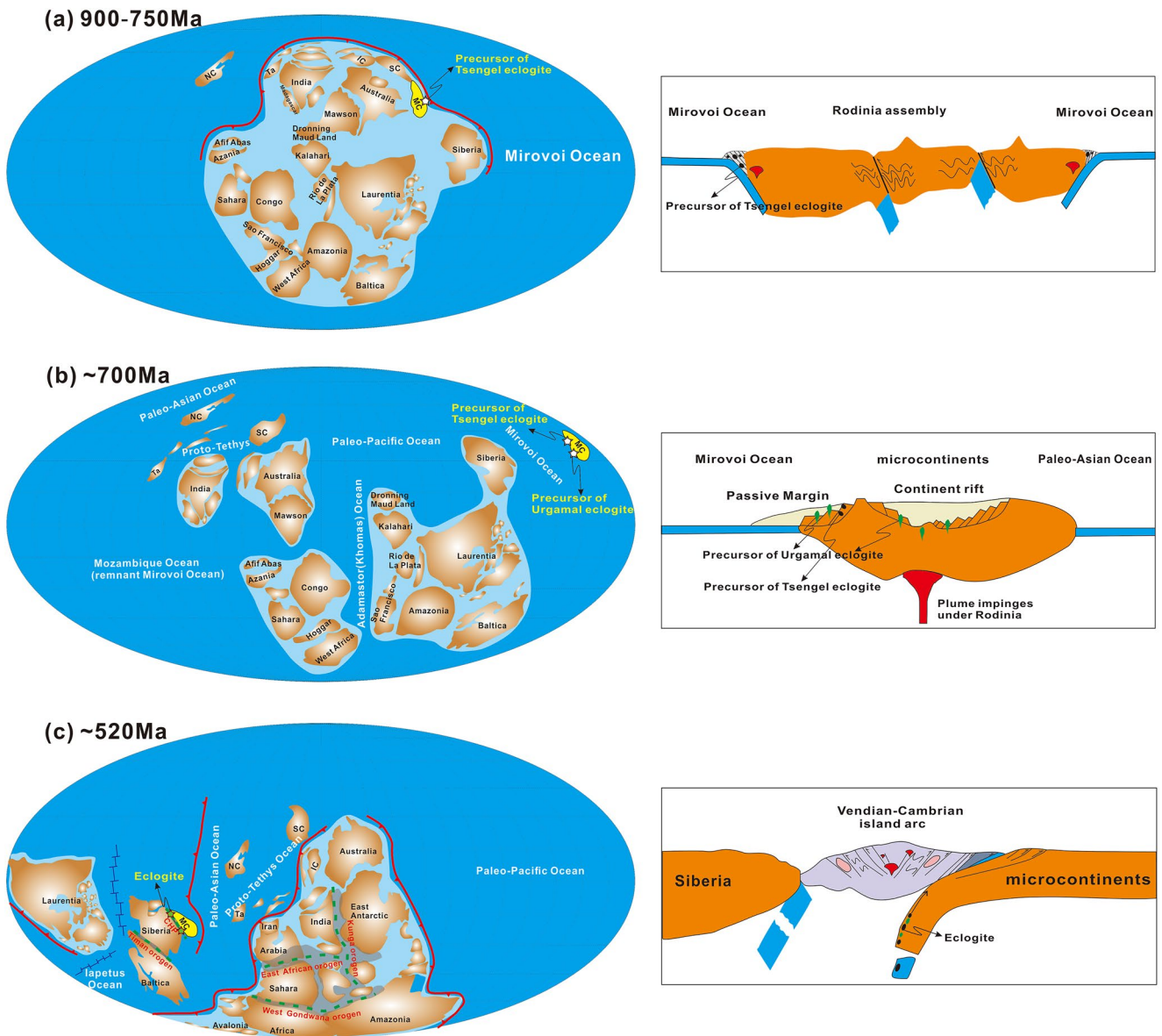


**Figure 13.** Schematic diagrams for the tectonic evolution of the CAOB during Neoproterozoic to Cambrian and its link to the supercontinent reconstruction (modified from Zhao et al. (2018)). MC, Microcontinents within the CAOB, CHP, Cambrian high-pressure metamorphic belt in the CAOB; NC, North China; SC, South China; Ta, Tarim; IC, Indochina.

widespread accumulation of Neoproterozoic passive margin clastic-carbonate sequence in southern Siberia and Zavkhan microcontinent of Mongolia (Bold, Crowley, et al., 2016; Gladkochub et al., 2019).

During 570–530 Ma, the subduction of the Mirovoi Ocean, rather than the newly formed Paleo-Asian oceans, likely led to the formation of the Ediacaran-Cambrian island arc. The divergence and expansion of the Paleo-Asian Ocean during Rodinia breakup would have reduced the size of the Mirovoi Ocean. The Cambrian HP eclogites demonstrate that the remnant Mirovoi Ocean between the CAOB microcontinents and island arcs closed at ~520 Ma as subduction continued. Another crustal block was likely involved in this accretionary event (Bold, Crowley, et al., 2016). A >1,000 km long Cambrian granulite-bearing metamorphic belt (~500 Ma) was reported at the southern margin of the Siberia (e.g., Gladkochub et al., 2008; Zhou et al., 2018), indicating the microcontinents probably accreted to the Siberian craton during the Cambrian. Such a scenario is supported by paleomagnetic data that indicate the CAOB microcontinents were adjacent to Siberia and the fact that both share a number of similar taxa during the Early Cambrian (Esakova & Zhegallo, 1996; Kravchinsky

et al., 2010). Metamorphism with similar ages has been widely reported within other parts of the CAOB, such as the >1,300 km granulite-bearing Khondalite Belt of NE China (~530–500 Ma; Y. Yang et al., 2022; Zhou et al., 2018), the >150 km Kokchetav continent-type eclogite-bearing (U)HP belt (~532 Ma; Zhang et al., 2016), the ~489 Ma Anrakhai metamorphic complex (Alexeiev et al., 2011), the ~474 Ma Aktuz eclogite-bearing metamorphic complex (Rojas-Agramonte et al., 2013) and the ~498–509 Ma Makbal eclogite-bearing metamorphic complex (Konopelko et al., 2012). These high-grade metamorphic rocks document the closure of the Mirovoi Ocean within the CAOB (Figure 13c). After the closure of the Mirovoi Ocean, the evolution of the Paleo-Asian Ocean dominated the development of the CAOB. The timing of the Mirovoi Ocean closure within CAOB is generally coincident with the final closure of the Mozambique Ocean and Mawson Ocean leading to the Gondwana assembly at ~550–530 Ma, which are also considered as part of the Pan-Rodinia Ocean (e.g., Merdith et al., 2021; Zhao et al., 2018). This coincidence means different branches of the Pan-Rodinia Ocean were closed nearly at the similar time interval worldwide.

## 6. Conclusions

Two newly discovered Cambrian HP eclogites in Mongolia provide key constraints for the Neoproterozoic-Cambrian tectonic evolution of the CAOB. They represent mafic rocks produced in a continental rift setting and early Neoproterozoic subduction-accretion complexes developed along the west margins of the microcontinents. We propose a tectonic model, in which the HP complexes are correlated, and form part of a >1,000 km long Cambrian HP metamorphic belt that was subjected to HP metamorphism when the microcontinents accreted to the Siberian Craton leading to the final closure of the Pan-Rodinia Mirovoi Ocean at ~520 Ma.

## Data Availability Statement

The data used are available in Supporting Information S1 and <https://doi.org/10.5281/zenodo.7220137>.

## References

- Aldanmaz, E., Pearce, J. A., Thirlwall, M. F., & Mitchell, J. G. (2000). Petrogenetic evolution of late Cenozoic, post-collision volcanism in western Anatolia, Turkey. *Journal of Volcanology and Geothermal Research*, 102(1–2), 67–95. [https://doi.org/10.1016/s0377-0273\(00\)00182-7](https://doi.org/10.1016/s0377-0273(00)00182-7)
- Alexeiev, D. V., Ryazantsev, A. V., Kröner, A., Tretyakov, A. A., Xia, X., & Liu, D. Y. (2011). Geochemical data and zircon ages for rocks in a high-pressure belt of Chu–Yili Mountains, southern Kazakhstan: Implications for the earliest stages of accretion in Kazakhstan and the Tianshan. *Journal of Asian Earth Sciences*, 42(5), 805–820. <https://doi.org/10.1016/j.jseae.2010.09.004>
- Anderson, L. J., & Smith, R. D. (1995). The effects of temperature and fO<sub>2</sub> on the Al in hornblende barometer. *American Mineralogist*, 80(5–6), 549–559. <https://doi.org/10.2138/am-1995-5-614>
- Badarch, G., Cunningham, D. W., & Windley, B. F. (2002). A new terrane subdivision for Mongolia: Implications for the Phanerozoic crustal growth of Central Asia. *Journal of Asian Earth Sciences*, 21(1), 87–110. [https://doi.org/10.1016/s1367-9120\(02\)00017-2](https://doi.org/10.1016/s1367-9120(02)00017-2)
- Bayarbold, M., Okamoto, A., Dandar, O., Uno, M., & Tsuchiya, N. (2022). Continental arc-derived eclogite in the Zavkhan Terrane, western Mongolia: Implications for the suture zone in the northern part of the Central Asian Orogenic Belt. *Journal of Asian Earth Sciences*, 229, 105150. <https://doi.org/10.1016/j.jseae.2022.105150>
- Bold, U., Crowley, J. L., Smith, E. F., Sambuu, O., & Macdonald, F. A. (2016). Neoproterozoic to early Paleozoic tectonic evolution of the Zavkhan terrane of Mongolia: Implications for continental growth in the Central Asian orogenic belt. *Lithosphere*, 8(6), 729–750. <https://doi.org/10.1306/549.1>
- Bold, U., Smith, E. F., Rooney, A. D., Bowring, S. A., Buchwaldt, R., Dudás, F. Ó., et al. (2016). Neoproterozoic stratigraphy of the Zavkhan terrane of Mongolia: The backbone for Cryogenian and early Ediacaran chemostratigraphic records. *American Journal of Science*, 316, 1–63. <https://doi.org/10.2475/01.2016.01>
- Bonin, B. (2004). Do coeval mafic and felsic magmas in post-collisional to within-plate regimes necessarily imply two contrasting, mantle and crustal, sources? A review. *Lithos*, 78(1–2), 1–24. <https://doi.org/10.1016/j.lithos.2004.04.042>
- Buriánek, D., Schulmann, K., Hrdličková, K., Hanžl, P., Janoušek, V., Gerdes, A., & Lexa, O. (2017). Geochemical and geochronological constraints on distinct Early-Neoproterozoic and Cambrian accretionary events along southern margin of the Baydrag Continent in western Mongolia. *Gondwana Research*, 47, 200–227. <https://doi.org/10.1016/j.gr.2016.09.008>
- Cao, W. T., Gilotti, J. A., Massonne, H. J., Ferrando, S., & Foster, C. T. J. (2019). Partial melting due to breakdown of an epidote-group mineral during exhumation of ultrahigh-pressure eclogite: An example from the North–East Greenland Caledonides. *Journal of Metamorphic Geology*, 37(1), 15–39. <https://doi.org/10.1111/jmg.12447>
- Cawood, P. A., Nemchin, A. A., Strachan, R., Prave, T., & Krabbendam, M. (2007). Sedimentary basin and detrital zircon record along East Laurentia and Baltica during assembly and breakup of Rodinia. *Journal of the Geological Society*, 164(2), 257–275. <https://doi.org/10.1144/0016-76492006-115>
- Compston, W., Williams, I. S., & Mayer, C. (1984). U–Pb geochronology of zircons from lunar breccia 73217 using a sensitive high resolution ion microprobe. *Journal of Geophysical Research*, 89(S02), B525–B534. <https://doi.org/10.1029/jb089is02p0525>
- Condie, K. C. (2002). The supercontinent cycle: Are there two patterns of cyclicity? *Journal of African Earth Sciences*, 35(2), 179–183. [https://doi.org/10.1016/s0899-5362\(02\)00005-2](https://doi.org/10.1016/s0899-5362(02)00005-2)
- Connolly, J. A. D. (2005). Computation of phase equilibria by linear programming: A tool for geodynamic modeling and its application to subduction zone decarbonation. *Earth and Planetary Science Letters*, 236(1–2), 524–541. <https://doi.org/10.1016/j.epsl.2005.04.033>

## Acknowledgments

We are grateful to Chun Yang, Mingzhu Ma, Liqin Zhou, Xiaochao Che, Lihui Jia, Chenghao Liu, Liangliang Huang, and Shuangrong Zhang for their supports of the analytical experiments, and to Jilei Li for insightful suggestions. We greatly appreciate the reviews by Brendan Murphy and Wentao Cao that significantly improved the paper. Editor-in-Chief Mark Dekkers and Associate Editor are thanked for the comments and the efficient editorial handling. We further thank Munkhtsengel Baatar and Chimedtsersen Anaad for their supports during our field investigations in Mongolia. This work was financially supported by Strategic Priority Research Program of Chinese Academy of Sciences (Grant XDB 41000000), the National Natural Science Foundation of China (Grant 42272262), the Second Tibetan Plateau Scientific Expedition and Research Program (Grant 2019QZKK0806) and Ramón y Cajal Fellowship from the Spanish Ministry of Science and Innovation (Grant RYC2019-028244-I).

- Dijkstra, A. H., Brouwer, F. M., Cunningham, W. D., Buchan, C., Badarch, G., & Mason, P. R. D. (2006). Late Neoproterozoic proto-arc ocean crust in the Dariv Range, Western Mongolia: A supra-subduction zone end-member ophiolite. *Journal of the Geological Society*, 163(2), 363–373. <https://doi.org/10.1144/0016-764904-156>
- Edel, J. B., Schulmann, K., Hanžl, P., & Lexa, O. (2014). Palaeomagnetic and structural constraints on 90° anticlockwise rotation in SW Mongolia during the Permo-Triassic: Implications for Altaid oroclinal bending. Preliminary palaeomagnetic results. *Journal of Asian Earth Sciences*, 94, 157–171. <https://doi.org/10.1016/j.jseas.2014.07.039>
- Ernst, R. E., Hamilton, M. A., Söderlund, U., Hanes, J. A., Gladkochub, D. P., Okrugin, A. V., et al. (2016). Long-lived connection between southern Siberia and northern Laurentia in the Proterozoic. *Nature Geoscience*, 9(6), 464–469. <https://doi.org/10.1038/ngeo2700>
- Esakova, N. V., & Zhegallo, E. A. (1996). *The biostratigraphy and fauna of the Early Cambrian in Mongolia* (p. 270). Nauka. (in Russian).
- Gale, A., Laubier, M., Escrig, S., & Langmuir, C. H. (2013). Constraints on melting processes and plume–ridge interaction from comprehensive study of the FAMOUS and North Famous segments, Mid-Atlantic Ridge. *Earth and Planetary Science Letters*, 365, 209–220. <https://doi.org/10.1016/j.epsl.2013.01.022>
- Gee, D. G., Janák, M., Majka, J., Robinson, P., & van Roermund, H. (2012). Subduction along and within the Baltoscandian margin during closing of the Iapetus Ocean and Baltica–Laurentia collision. *Lithosphere*, 5(2), 169–178. <https://doi.org/10.1130/L220.1>
- Gladkochub, D. P., Donskaya, T. V., Stanevich, A. M., Pisarevsky, S. A., Zhang, S., Motova, Z. L., et al. (2019). U–Pb detrital zircon geochronology and provenance of Neoproterozoic sedimentary rocks in southern Siberia: New insights into breakup of Rodinia and opening of Paleo-Asian Ocean. *Gondwana Research*, 65, 1–16. <https://doi.org/10.1016/j.gr.2018.07.007>
- Gladkochub, D. P., Donskaya, T. V., Wingate, M. T. D., Poller, U., Kroner, A., Fedorovsky, V. S., et al. (2008). Petrology, geochronology, and tectonic implications of c. 500 Ma metamorphic and igneous rocks along the northern margin of the Central Asian Orogen (Olkhon terrane, Lake Baikal, Siberia). *Journal of the Geological Society*, 165(1), 235–246. <https://doi.org/10.1144/0016-76492006-125>
- Gordienko, I. V., Bulgatov, A. N., Ruzhentsev, S. V., Minina, O. R., Klimuk, V. S., Vetluzhskikh, L. I., et al. (2010). The Late Riphean–Paleozoic history of the Uda–Vitim island arc system in the Transbaikalian sector of the Paleozoic ocean. *Russian Geology and Geophysics*, 51(5), 461–481. <https://doi.org/10.1016/j.rgg.2010.04.005>
- Gordienko, I. V., Filimonov, A. V., Minina, O. R., Gornova, M. A., Medvedev, A. Y., Klimuk, V. S., et al. (2007). Dzhida island–arc system in the Paleozoic Ocean: Structure and main stages of Vendian–Paleozoic geodynamic evolution. *Russian Geology and Geophysics*, 48(1), 91–106. <https://doi.org/10.1016/j.rgg.2006.12.009>
- Gordienko, I. V., Gorokhovskiy, D. V., Elbaev, A. L., & Bayanova, T. B. (2015). New data on the Early Paleozoic gabbroid and granitoid magmatism age within the Dzhida zone of Caledonides (Southwestern Transbaikalia, North Mongolia). *Doklady Earth Sciences*, 463(2), 817–821. <https://doi.org/10.1134/S1028334X15080103>
- Hermann, J., & Rubatto, D. (2014). Subduction of continental crust to mantle depth: Geochemistry of ultrahigh-pressure rocks. *Treatise on Geochemistry*, 4, 309–340.
- Hoffman, P. F. (1991). Did the breakout of Laurentia turn Gondwanaland inside–out? *Science*, 252(5011), 1409–1412. <https://doi.org/10.1126/science.252.5011.1409>
- Holland, T., & Blundy, J. (1994). Non-ideal interactions in calcic amphiboles and their bearing on amphibole–plagioclase thermometry. *Contributions to Mineralogy and Petrology*, 116(4), 433–447. <https://doi.org/10.1007/bf00310910>
- Holland, T. J. B., & Powell, R. (2011). An improved and extended internally consistent thermodynamic dataset for phases of petrological interest, involving a new equation of state for solids. *Journal of Metamorphic Geology*, 29(3), 333–383. <https://doi.org/10.1111/j.1525-1314.2010.00923.x>
- Hoskin, P. W. O., & Black, L. P. (2000). Metamorphic zircon formation by solid–state re–crystallization of protolith igneous zircon. *Journal of Metamorphic Geology*, 18(4), 423–439. <https://doi.org/10.1046/j.1525-1314.2000.00266.x>
- Hoskin, P. W. O., & Schaltegger, U. (2003). The composition of zircon and igneous and metamorphic petrogenesis. In J. M. Hancher & P. W. O. Hoskin (Eds.), *Zircon* (Vol. 53, pp. 27–62).
- Jackson, S. E., Pearson, N. J., Griffin, W. L., & Belousova, E. A. (2004). The application of laser ablation–inductively coupled plasma–mass spectrometry to in situ U–Pb zircon geochronology. *Chemical Geology*, 211(1–2), 47–69. <https://doi.org/10.1016/j.chemgeo.2004.06.017>
- Janoušek, V., Jiang, Y., Buriánek, D., Schulmann, K., Hanžl, P., Soejono, I., et al. (2018). Cambrian–ordovician magmatism of the Ikh–Mongol Arc system exemplified by the Khantaishir Magmatic Complex (Lake Zone, south–central Mongolia). *Gondwana Research*, 54, 122–149. <https://doi.org/10.1016/j.gr.2017.10.003>
- Jian, P., Kröner, A., Jahn, B. –m., Windley, B. F., Shi, Y., Zhang, W., et al. (2014). Zircon dating of Neoproterozoic and Cambrian ophiolites in West Mongolia and implications for the timing of orogenic processes in the central part of the Central Asian Orogenic Belt. *Earth Science Review*, 133, 62–93. <https://doi.org/10.1016/j.earscirev.2014.02.006>
- Khain, E. V., Bibikova, E. V., Kröner, A., Zhuravlev, D. Z., Sklyarov, E. V., Fedotova, A. A., & Kravchenko–Berezhnoy, I. R. (2002). The most ancient ophiolite of the Central Asian fold belt: U–Pb and Pb–Pb zircon ages for the Dunzhugur Complex, Eastern Sayan, Siberia, and geodynamic implications. *Earth and Planetary Science Letters*, 199(3–4), 311–325. [https://doi.org/10.1016/S0012-821X\(02\)00587-3](https://doi.org/10.1016/S0012-821X(02)00587-3)
- Khain, E. V., Bibikova, E. V., Salnikova, E. B., Kröner, A., Gibsher, A. S., Didenko, A. N., et al. (2003). The Palaeo–Asian ocean in the Neoproterozoic and early Palaeozoic: New geochronologic data and palaeotectonic reconstructions. *Precambrian Research*, 122(1–4), 329–358. [https://doi.org/10.1016/S0301-9268\(02\)00218-8](https://doi.org/10.1016/S0301-9268(02)00218-8)
- Kohn, M. J. (2020). A refined zirconium–in–rutile thermometer. *American Mineralogist*, 105(6), 963–971. <https://doi.org/10.2138/am-2020-7091>
- Konopelko, D., Kullerud, K., Apayarov, F., Sakiev, K., Baruleva, O., Ravna, E., & Lepekina, E. (2012). SHRIMP zircon chronology of HP–UHP rocks of the Makbal metamorphic complex in the Northern Tien Shan, Kyrgyzstan. *Gondwana Research*, 22(1), 300–309. <https://doi.org/10.1016/j.gr.2011.09.002>
- Kovach, V., Kozakov, I., Kröner, A., Salnikova, E., Wang, K. L., Lee, H. Y., et al. (2021). Early Neoproterozoic crustal growth and microcontinent formation of the north–central Central Asian Orogenic Belt: New geological, geochronological, and Nd–Hf isotopic data on the M’elange Zone within the Zavkhan terrane, western Mongolia. *Gondwana Research*, 91, 254–276. <https://doi.org/10.1016/j.gr.2020.12.022>
- Kozakov, I., Kozlovsky, A., Yarmolyuk, V., Kovach, V., Bibikova, E., Kirnozova, T., et al. (2011). Crystalline complexes of the Tarbagatai block of the Early Caledonian superterrane of Central Asia. *Petrology*, 19(4), 426–444. <https://doi.org/10.1134/S0869591111040047>
- Kravchinsky, V. A., Sklyarov, E. V., Gladkochub, D. B., & Harbert, W. P. (2010). Paleomagnetism of the Precambrian Eastern Sayan rocks: Implications for the Ediacaran–Early Cambrian paleogeography of the Tuva–Mongolian composite terrane. *Tectonophysics*, 486(1–4), 65–80. <https://doi.org/10.1016/j.tecto.2010.02.010>
- Kröner, A., Kovach, V., Kozakov, I., Kirnozova, T., Azimov, P., Wong, J., & Geng, H. (2015). Zircon ages and Nd–Hf isotopes in UHT granulites of the Ider Complex: A cratonic terrane within the Central Asian Orogenic Belt in NW Mongolia. *Gondwana Research*, 27(4), 1392–1406. <https://doi.org/10.1016/j.gr.2014.03.005>

- Kuzmichev, A. B., & Larionov, A. N. (2011). The Sarkhoi Group in East Sayan: Neoproterozoic (similar to 770–800 Ma) volcanic belt of the Andean type. *Russian Geology and Geophysics*, 52(7), 685–700. <https://doi.org/10.1016/j.rgg.2011.06.001>
- Kuzmichev, A. V., Kröner, A., Hegner, E., Dunyi, L., & Yusheng, W. (2005). The Shishkhdid ophiolite, northern Mongolia: A key to the reconstruction of a Neoproterozoic island–arc system in central Asia. *Precambrian Research*, 138(1–2), 125–150. <https://doi.org/10.1016/j.precamres.2005.04.002>
- Lehmann, J., Schulmann, K., Lexa, O., Corsini, M., Kroner, A., Stipska, P., et al. (2010). Structural constraints on the evolution of the Central Asian Orogenic Belt in SW Mongolia. *American Journal of Science*, 310(7), 575–628. <https://doi.org/10.2475/07.2010.02>
- Levashova, N. M., Kalugin, V. M., Gibsher, A. S., Yff, J., Ryabinin, A. B., Meert, J. G., & Malone, S. J. (2010). The origin of the Baydaric microcontinent, Mongolia: Constraints from paleomagnetism and geochronology. *Tectonophysics*, 485(1–4), 306–320. <https://doi.org/10.1016/j.tecto.2010.01.012>
- Levashova, N. M., Meert, J. G., Gibsher, A. S., Grice, W. C., & Bazheniv, M. L. (2011). The origin of microcontinents in the Central Asian Orogenic Belt: Constraints from paleomagnetism and geochronology. *Precambrian Research*, 185(1–2), 37–54. <https://doi.org/10.1016/j.precamres.2010.12.001>
- Li, P., Sun, M., Narantsetseg, T., Jourdan, F., Hu, W., & Yuan, C. (2022). First structural observation around the hinge of the Mongolian Orocline (Central Asia): Implications for the geodynamics of oroclinal bending and the evolution of the Mongol–Okhotsk Ocean. *Geological Society of America Bulletin*, 134(7–8), 1994–2006. <https://doi.org/10.1130/b36200.1>
- Li, Z. X., Bogdanova, S. V., Collins, A. S., Davidson, A., De Waele, B., Ernst, R. E., et al. (2008). Assembly, configuration, and break-up history of Rodinia: A synthesis. *Precambrian Research*, 160(1–2), 179–210. <https://doi.org/10.1016/j.precamres.2007.04.021>
- Ludwig, K. R. (2001). *Squid 1.03 A User's Manual* (Vol. 2). Berkeley Geochronology Center Special Publication.
- Ludwig, K. R. (2003). *User's Manual for Isoplot 3.0. A geochronological toolkit for Microsoft Excel* (Vol. 4). Berkeley Geochronology Center Special Publication.
- Macdonald, F. A., Jones, D. S., & Schrag, D. P. (2009). Stratigraphic and tectonic implications of a newly discovered glacial diamictite–cap carbonate couplet in southwestern Mongolia. *Geology*, 37(2), 123–126. <https://doi.org/10.1130/g24797a.1>
- Massonne, H.-J. (2013). Constructing the pressure–temperature path of ultrahigh-pressure rocks. *Elements*, 9(4), 267–272. <https://doi.org/10.2113/gselements.9.4.267>
- Merdith, A. S., Williams, S. E., Collins, A. S., Tetley, M. G., Mulder, J. A., Blades, M. L., et al. (2021). Extending full–plate tectonic models into deep time: Linking the Neoproterozoic and the Phanerozoic. *Earth-Science Reviews*, 214, 103477. <https://doi.org/10.1016/j.earscirev.2020.103477>
- Meschede, M. (1986). A method of discriminating between different types of midocean ridge basalts and continental tholeiites with the Nb–Zr–Y diagram. *Chemical Geology*, 56(3–4), 207–218. [https://doi.org/10.1016/0009-2541\(86\)90004-5](https://doi.org/10.1016/0009-2541(86)90004-5)
- Mitchell, R. N., Zhang, N., Salminen, J., Liu, Y., Spencer, C. J., Steinberger, B., et al. (2021). The supercontinent cycle. *Nature Reviews Earth & Environment*, 2(5), 358–374. <https://doi.org/10.1038/s43017-021-00160-0>
- Murphy, J. B., & Nance, R. D. (2003). Do supercontinents introvert or extrovert?: Sm–Nd isotope evidence. *Geology*, 31(10), 873–876. <https://doi.org/10.1130/g19668.1>
- Nance, R. D., Murphy, J. B., & Santosh, M. (2014). The supercontinent cycle: A retrospective essay. *Gondwana Research*, 25(1), 4–29. <https://doi.org/10.1016/j.gr.2012.12.026>
- Palin, R. M., Weller, O. M., Waters, D. J., & Dyck, B. (2016). Quantifying geological uncertainty in metamorphic phase equilibria modeling: a Monte Carlo assessment and implications for tectonic interpretations. *Geoscience Frontiers*, 7(4), 591–607. <https://doi.org/10.1016/j.gsf.2015.08.005>
- Parfenov, L. M., Khanchuk, A. I., Badarch, G., Miller, R. J., Naumova, V. V., Nokleberg, W. J., et al. (2003). Preliminary Northeast Asia geodynamics map, sheet 2, scale 1:5,000,000. *US Geological Survey Open–File Report 03–205*.
- Pastor-Galán, D., Nance, R. D., Murphy, J. B., & Spencer, C. J. (2019). Supercontinents: Myths, mysteries, and milestones. *Geological Society, London, Special Publications*, 470(1), 39–64. <https://doi.org/10.1144/sp470.16>
- Pearce, J. A. (2008). Geochemical fingerprinting of oceanic basalts with applications to ophiolite classification and the search for Archean oceanic crust. *Lithos*, 100(1–4), 14–48. <https://doi.org/10.1016/j.lithos.2007.06.016>
- Pearce, J. A., & Norry, M. J. (1979). Petrogenetic implications of Ti, Zr, Y, and Nb variations in volcanic rocks. *Contributions to Mineralogy and Petrology*, 69(1), 33–47. <https://doi.org/10.1007/bf00375192>
- Ravna, E. J. K. (2000). The garnet–clinopyroxene Fe<sup>2+</sup>–Mg geothermometer: An updated calibration. *Journal of Metamorphic Geology*, 18(2), 211–219. <https://doi.org/10.1046/j.1525-1314.2000.00247.x>
- Rojas-Agramonte, Y., Herwartz, D., García-Casco, A., Kröner, A., Alexeiev, D. V., Klemd, R., et al. (2013). Early Palaeozoic deep subduction of continental crust in the Kyrgyz North Tianshan: Evidence from Lu–Hf garnet geochronology and petrology of mafic dikes. *Contributions to Mineralogy and Petrology*, 166(2), 525–543. <https://doi.org/10.1007/s00410-013-0889-y>
- Rollinson, H. R. (1993). *Using geochemical data: Evaluation, presentation, interpretation* (p. 352). Longman Science and Technical.
- Rytsk, E. Y., Amelin, Y. V., Rizvanova, N. G., Krymskii, R. S., Mitrofanov, G. L., Mitrofanova, N. N., et al. (2001). Age of rocks in the Baikal–Muya foldbelt. *Stratigraphy and Geological Correlation*, 9, 315–326.
- Şengör, A. M. C., Natal'in, B. A., & Burtman, U. S. (1993). Evolution of the Altaid tectonic collage and Paleozoic crustal growth in Eurasia. *Nature*, 364(6435), 299–307. <https://doi.org/10.1038/364299a0>
- Simonov, V. A., Gordienko, I. V., Stupakov, S. I., Medvedev, A. Y., Kotlyarov, A. V., & Kovyazin, S. V. (2014). Conditions of basalt formation in the Dzhida zone of the Paleoasian Ocean. *Russian Geology and Geophysics*, 55(8), 929–940. <https://doi.org/10.1016/j.rgg.2014.07.001>
- Skuzovatov, S. (2021). Nature and (in-) coherent metamorphic evolution of subducted continental crust in the Neoproterozoic accretionary collage of SW Mongolia. *Geoscience Frontiers*, 12(3), 101097. <https://doi.org/10.1016/j.gsf.2020.10.004>
- Skuzovatov, S. Y., Shatsky, V. S., Dril, S. I., & Perepelov, A. B. (2018). Elemental and isotopic (Nd–Sr–O) geochemistry of eclogites from the Zamtyun–Nuruu area (SW Mongolia): Crustal contribution and relation to Neoproterozoic subduction–accretion events. *Journal of Asian Earth Sciences*, 167, 33–51. <https://doi.org/10.1016/j.jseae.2017.11.032>
- Sláma, J., Kosler, J., Condon, D. J., Crowley, J. L., Gerdes, A., Hanchar, J. M., et al. (2008). Plesovice zircon—A new natural reference material for U–Pb and Hf isotopic microanalysis. *Chemical Geology*, 249(1–2), 1–35. <https://doi.org/10.1016/j.chemgeo.2007.11.005>
- Štípská, P., Schulmann, K., Lehmann, J., Corsini, M., Lexa, O., & Tomurhuu, D. (2010). Early Cambrian eclogites in SW Mongolia: Evidence that the Palaeo–Asian Ocean suture extends further east than expected. *Journal of Metamorphic Geology*, 28(9), 915–933. <https://doi.org/10.1111/j.1525-1314.2010.00899.x>
- Sun, S. S., & McDonough, W. F. (1989). Chemical and isotopic systematics of oceanic basalts; implications for mantle composition and processes. In A. D. Saunders & M. J. Norry (Eds.), *Magmatism in the ocean basins* (Vol. 42, pp. 313–345). Geological Society Special Publications.

- Tomurhuu, D., Bolorjargal, P., & Jian, P. (2007). New dating and geochemistry of Dzhida boninite series rocks and its tectonic constrain. In *Abstract and Excursion Guide Book of the 3rd International Workshop and Field Excursion for IGCP-480* (p. 33).
- Tsujimori, T., Sisson, V. B., Liou, J. G., Harlow, G. E., & Sorensen, S. S. (2006). Very-low-temperature record of the subduction process: A review of worldwide lawsonite eclogites. *Lithos*, 92(3–4), 609–624. <https://doi.org/10.1016/j.lithos.2006.03.054>
- Vervoort, J. D., Patchett, P. J., Blichert-Toft, J., & Albarede, F. (1999). Relationships between Lu–Hf and Sm–Nd isotopic systems in the global sedimentary system. *Earth and Planetary Science Letters*, 168(1–2), 79–99. [https://doi.org/10.1016/S0012-821X\(99\)00047-3](https://doi.org/10.1016/S0012-821X(99)00047-3)
- Wakabayashi, J. (2017). Structural context and variation of ocean plate stratigraphy, Franciscan Complex, California: Insight into melange origins and subduction–accretion processes. *Progress in Earth and Planetary Science*, 4(1), 18. <https://doi.org/10.1186/s40645-017-0132-y>
- Waters, D. J., & Martin, H. N. (1993). Geobarometry of phengite-bearing eclogites. *Terra Abstracts*, 5, 410–411.
- Waters, D. J., & Martin, H. N. (1996). The garnet–Cpx–phengite barometer. *Recommended calibration and calculation method*. Retrieved from <http://www.earth.ox.ac.uk/~davewa/research/eclogites/ecbarcal.html>
- Wei, C. J., & Clarke, G. L. (2011). Calculated phase equilibria for MORB compositions: A reappraisal of the metamorphic evolution of lawsonite eclogite. *Journal of Metamorphic Geology*, 29(9), 939–952. <https://doi.org/10.1111/j.1525-1314.2011.00948.x>
- Wen, B., Evans, D. A. D., Wang, C., Li, Y. –X., & Jing, X. (2018). A positive test for the Greater Tarim Block at the heart of Rodinia: Mega-dextral suturing of supercontinent assembly. *Geology*, 46(8), 687–690. <https://doi.org/10.1130/g40254.1>
- Whitney, D. L., & Davis, P. B. (2006). Why is lawsonite eclogite so rare? Metamorphism and preservation of lawsonite eclogite, Sivrihisar, Turkey. *Geology*, 34(6), 473–476. <https://doi.org/10.1130/g22259.1>
- Wilhem, C., Windley, B. F., & Stampfli, G. M. (2012). The Altaids of Central Asia: A tectonic and evolutionary innovative review. *Earth Science Review*, 113(3–4), 303–341. <https://doi.org/10.1016/j.earscirev.2012.04.001>
- Williams, I. S. (1998). U–Th–Pb geochronology by ion microprobe. In M. A. McKibben, W. C. Shanks III, & W. I. Ridley (Eds.), *Applications of microanalytical techniques to understanding mineralizing processes, Reviews in economic geology* (Vol. 7, pp. 1–35).
- Wilson, M. (1989). *Igneous petrogenesis: A global tectonic approach* (p. 466). Springer.
- Windley, B. F., Alexeev, D., Xiao, W. J., Kroner, A., & Badarch, G. (2007). Tectonic models for accretion of the Central Asian Orogenic Belt. *Journal of the Geological Society*, 164(1), 31–47. <https://doi.org/10.1144/0016-76492006-022>
- Xia, L., & Li, X. M. (2019). Basalt geochemistry as a diagnostic indicator of tectonic setting. *Gondwana Research*, 65, 43–67. <https://doi.org/10.1016/j.gr.2018.08.006>
- Xiao, W. J., Windley, B. F., Sun, S., Li, J., Huang, B. C., Han, C. M., et al. (2015). A tale of amalgamation of three Permo–Triassic collage systems in Central Asia: Oroclines, sutures, and terminal accretion. *Annual Review of Earth and Planetary Sciences*, 43(1), 477–507. <https://doi.org/10.1146/annurev-earth-060614-105254>
- Yang, H., Xu, W. L., Sorokin, A. A., Ovchinnikov, R. O., & Ge, W. H. (2020). Geochronology and geochemistry of Neoproterozoic magmatism in the Bureya Block, Russian Far East: Petrogenesis and implications for Rodinia reconstruction. *Precambrian Research*, 342, 105676. <https://doi.org/10.1016/j.precamres.2020.105676>
- Yang, Y., Liang, C. Y., Zheng, C. Q., Xu, X. C., Zhou, X., & Hu, P. Y. (2022). The metamorphic characteristics of metapelites of the Mashan Group in Mashan area, eastern Heilongjiang Province, China: Constraint on the crustal evolution of the Jiamusi Massif. *Gondwana Research*, 102, 299–331. <https://doi.org/10.1016/j.gr.2020.10.004>
- Yang, Y., Zhang, H., Chu, Z., Xie, L., & Wu, F. (2010). Combined chemical separation of Lu, Hf, Rb, Sr, Sm and Nd from a single rock digest and precise and accurate isotope determinations of Lu–Hf, Rb–Sr and Sm–Nd isotope systems using Multi–Collector ICP–MS and TIMS. *International Journal of Mass Spectrometry*, 290(2–3), 120–126. <https://doi.org/10.1016/j.ijms.2009.12.011>
- Yarmolyuk, V. V., Kovach, V. P., Kovalenko, V. I., Salnikova, E. B., Kozlovskii, A. M., Kotov, A. B., et al. (2011). Composition, sources, and mechanism of continental crust growth in the Lake Zone of the Central Asian Caledonides: I. Geological and geochronological data. *Petrology*, 19(1), 55–78. <https://doi.org/10.1134/S0869591111010085>
- Zhang, R. Y., Li, X. H., Yui, T. F., Jahn, B. M., Liou, J. G., & Ling, X. X. (2016). U–Pb geochronology of zircon and rutile from the Kokchetav metamorphic belt, northern Kazakhstan and its tectonic implications. *European Journal of Mineralogy*, 28(6), 1203–1213. <https://doi.org/10.1127/ejm/2016/0028-2523>
- Zhao, G., Wang, Y., Huang, B., Dong, Y., Li, S., Zhang, G., & Yu, S. (2018). Geological reconstructions of the East Asian blocks: From the breakup of Rodinia to the assembly of Pangea. *Earth-Science Reviews*, 186, 262–286. <https://doi.org/10.1016/j.earscirev.2018.10.003>
- Zhao, J.-H., & Zhou, M.-F. (2008). Neoproterozoic adakitic plutons in the northern margin of the Yangtze Block, China: Partial melting of a thickened lower crust and implications for secular crustal evolution. *Lithos*, 104(1–4), 231–248. <https://doi.org/10.1016/j.lithos.2007.12.009>
- Zheng, Y. F., Xia, Q. X., Chen, R. X., & Gao, X. Y. (2011). Partial melting, fluid supercriticality and element mobility in ultrahigh-pressure metamorphic rocks during continental collision. *Earth-Science Reviews*, 107(3–4), 342–374. <https://doi.org/10.1016/j.earscirev.2011.04.004>
- Zhou, J.-B., Wilde, S. A., Zhao, G.-C., & Han, J. (2018). Nature and assembly of microcontinental blocks within the Paleo–Asian Ocean. *Earth-Science Reviews*, 186, 76–93. <https://doi.org/10.1016/j.earscirev.2017.01.012>